Macromolecules

pubs.acs.org/Macromolecules Article

Connecting Features of Ionomer Scattering Profiles to the Real-Space Structural Features of Ionomer Domains

Jason J. Madinya, Stephen Kronenberger, Benjamin Gould, Colin Peterson, and Arthi Jayaraman*

Cite This: *Macromolecules* 2024, 57, 8223−8239 Read Online

ACCESS | Metrics & More | Article Recommendations | Supporting Information

ABSTRACT: Membranes made of hydrated ionomers are frequently used in ion-exchange applications, such as hydrogen fuel cells and water electrolyzers. Perfluorinated sulfonic acid (PFSA) ionomer membranes are suited for these applications as they possess chemical stability and mechanical stability at elevated pressures and temperatures and have ion transport capabilities. Hydrated PFSA ionomers form a nanophase-separated structure that has an ion-conducting hydrophilic phase and a nonconducting, semicrystalline hydrophobic phase. This complex nanophase structure of hydrated ionomers is a topic of great interest, and there have been a number of studies attempting to elucidate the morphology of hydrated ionomers by using microscopy, simulations, and scattering measurements. In this work, we seek to understand the connection between the ionomer design and the resulting nanophase structure under various hydration conditions using coarse-grained molecular simulations. We study the effects of varying the side chain spacing and side chain lengths on the measured scattering profiles and real-space hydrophilic domain properties. To enable correct real-space interpretation of the scattering measurement structure, we relate features observed in the scattering profiles, such as the ionomer peak location and intensity, to the hydrophilic domain size distribution, tortuosity, and onset of percolation. We also show how new ionomer designs with tailored variations in side chain spacing and side chain length affect domain size distributions and connectivity of the hydrophilic domains.

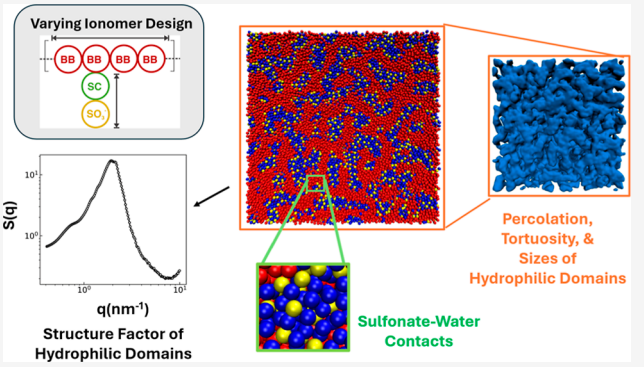

1. INTRODUCTION

Ionomers are charged copolymers composed of a polymer backbone, with a modest fraction of the monomers along the backbone having a charged pendant group.[1] Ionomers have lower charge density along the backbone as compared to polyelectrolytes, which are typically homopolymers with high linear charge density. Due to their lower charge density, ionomers self-assemble into nanostructures that are different from polyelectrolytes.[2] Electrostatic and van der Waals interactions and entropy dictate the features of the nanophase-separated structures in the melt[3−5] and hydrated states.[6−11] Due to these nanostructures, ionomers have drawn considerable interest for a variety of applications, including coatings,[12−14] shape-memory materials,[15,16] and drug delivery vehicles.[17−19] Additionally, the ion-conducting ability resulting from phase-separated hydrophilic and hydrophobic domains makes ionomers ideal for applications in hydrogen fuel cells,[20−24] electrolysis,[25−27] redox-flow batteries,[28−30] and separation processes.[31,32]

Among the variety of ionomer chemistries, perfluorinated sulfonic acid (PFSA) ionomers have been used extensively for developing ion-conductive membranes.[33] In particular, Nafion PFSA is well-studied for membrane applications.[34] To optimize PFSA ionomers for membrane applications, there is a need to identify ionomer designs that have the potential to facilitate high proton conductivity in the membrane and improved membrane mechanical properties. One such ionomer design parameter is the equivalent weight, (EW) defined as the ratio of the mass of dry polymer to the number of moles of sulfonate end groups (in units of g/mol). The EW of the ionomer can be altered by varying either the grafting density or length of the side chains the sulfonate end groups are attached to. Water content within the membrane is quantified by the parameter λ, defined as the ratio of the number of water molecules to the number of sulfonate end groups $\lambda = [H_2O]/[SO_3^-]$. Thus, for optimizing ionomers for membrane applications, both the hydrophilic and the hydrophobic domains must be tuned or tailored for the desired performance properties.

Structural characterization of the hydrophilic and hydrophobic domains using transmission electron microscopy[11,35−38] has limitations associated with poor image contrast and sample thickness. In contrast, small and wide-angle X-ray scattering

Received: April 30, 2024
Revised: July 30, 2024
Accepted: August 1, 2024
Published: August 19, 2024

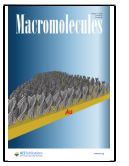

https://doi.org/10.1021/acs.macromol.4c00988
Macromolecules 2024, 57, 8223−8239

(WAXS) and neutron scattering measurements[33,39] have been more useful in understanding the complex nanostructure in ionomer membranes. Small-angle scattering measurements show a broad characteristic peak known as the "ionomer peak", which is attributed to the length scales between the hydrophilic domains on the order of several nanometers. A "matrix knee" in the scattering profile at lower-q values is due to the spacing between crystalline regions in the hydrophobic domains.[40−43] WAXS experiments show the scattering peak associated with the crystalline regions in the high-q range.[43] Despite certain aspects of PFSA ionomer structure being well-understood, the interpretation of these scattering profiles, specifically the ionomer peak, is nontrivial. The ionomer peak requires interpretation by fitting existing models to relate to real-space structural features. A variety of models have been proposed to explain the ionomer peak's presence, ranging from ionic clusters connected by thin hydrophilic domains to lamellae, to cylindrical channels, and to random network morphologies. It is not obvious a priori what types of models one needs to consider for fitting to the scattering profiles. Some knowledge of spatial arrangements in real space, the very question one wishes to answer in these ionomer systems, is needed to select any models for analyzing scattering profiles. Molecular simulations have been used to gain this knowledge of the real-space structural arrangements of the ionomers. We summarize a few of these simulation studies next to share the insights gained from them and the limitations they face that motivate the work presented in this paper.

Kuo et al.[44] performed all-atom molecular dynamics simulations of membranes based on Flemion (EW = 844 g/mol equiv) and Nafion (EW = 1144 g/mol equiv), with the water content ranging from λ = 1 to λ = 20. The EW was increased by adding more CF_2-units in the backbone while maintaining the same number of CF_2-units in the side chain, thus increasing the linear spacing between the side chains along the polymer backbone. They found that the hydrophilic domains become percolated at λ = 3, and as λ increases beyond 3, the morphology changes from a channel-network structure to a tortuous layer structure. They also report that the increasing EW leads to a more heterogeneous morphology. In another study, Kuo et al.[45] found that the longer side chain lengths caused aggregation of the aqueous domains, leading to a swollen network structure at high λ compared to the tortuous layer structure seen with shorter side chains at high λ. Due to the atomistic model used in these two simulation studies, the majority of the systems studied were limited to 13 nm or smaller in size as larger simulation box sizes at atomistic resolution become computationally demanding. As such, a study with a broad range of ionomer designs in larger systems, which is required to compare the scattering features that are related to larger length scales, becomes computationally infeasible.

To achieve larger length scales, Liu et al.[46] used dissipative particle dynamics (DPD) to quantify the morphology and growth of the hydrophilic domains in Nafion at varying λ values. They find the onset of percolation of the hydrophilic domains at λ = 5, and as λ was increased, the clusters grew from small aggregates to larger spheres, to elongated rods, and to branched twisted cylinders. DPD simulations have provided critical insights into the morphology of hydrated ionomers in a computationally efficient manner; however, the DPD approach is the highest level of coarse-graining (among molecular simulation methods), and it lacks excluded volume interactions due to the use of soft forces.

While the above simulation studies have all been valuable in understanding PFSA ionomer morphology, the connection between the length scales accessed in scattering experiments and simulations is still lacking, specifically, a direct link between features of the measured scattering profiles and their corresponding real-space structural description of domains. To compare the structure factors calculated from simulations to the scattering measurements in experiments, one needs a large simulation box and system size to capture the experimentally relevant length scales (0.1 nm to 1 μm) in the scattering profiles calculated from simulations. While the larger length scales (>100 nm) are not feasible with atomistic simulations, the smaller length scales (<1 nm) are missed in DPD simulations. However, the chemical details to capture water−sulfonate and water−polymer backbone arrangements driven by their electrostatic and van der Waals interactions with the potential role of polarizability are important to capture; this would not be possible with the DPD simulations described above. Thus, we need a model that can be used in large-scale simulations (hundreds of nm) while also maintaining essential chemical details of the polymer and with explicit representation of water molecules, including polarizability. In this regard, MARTINI models seem to be the optimal choice. MARTINI models have been used extensively for simulating biomacromolecules where the chemistry of the macromolecule and their interactions with water are critical for the structural arrangements of the biomolecules.[47−49] Mabuchi and Tokumasu[50] have demonstrated the use of the MARTINI v2 model for ionomers along with the refined polarizable water model developed by Michalowsky and co-workers[51] to study Nafion in solutions of water and 1-propanol mixtures[50,52,53] and the morphology of ionomer thin films under solvent evaporation.[54] One should note that while these coarse-grained (CG) MARTINI v2 ionomer models have been used to model the structure of hydrated Nafion membranes, they are not optimized to form crystalline domains of the PTFE backbone. Keeping that in mind, we adopt this MARTINI v2 ionomer model[56] with the refined polarizable water model[51] for our current simulation work aimed at connecting various aspects of ionomer design and blending designs to their self-assembled *amorphous* structure starting from random disordered initial configurations. We then relate features of the calculated scattering profiles (e.g., peak position and breadth) to real-space domain analysis (e.g., connectivity, domain sizes, and tortuosity) as a way to guide experimentalists who wish to connect their scattering profile features to real-space structural arrangements. After establishing this relationship between features of scattering profiles and real-space structural features, we then predict the effects of tailored new ionomer designs on the morphology, quantified by scattering profiles, as well as real-space domain analysis.

An aspect of PFSA ionomers that has not been well-explored in previous simulation studies is the effect of dispersity either by deliberately mixing ionomers with different EWs and/or different side-chain lengths or by creating ionomers with variations in side chain spacing and length along the chain. On the one hand, real polymers are rarely monodisperse, and determining whether this dispersity has any effect on the morphology of ionomer membranes can provide additional ties from the simulated system to experimental ionomer membranes. On the other hand, intentionally blending ionomers of differing design (side chain spacing and side chain length) could provide unique morphologies. In this work, we simulate both ionomers with different distributions of side chain spacing and blends of

https://doi.org/10.1021/acs.macromol.4c00988
Macromolecules 2024, 57, 8223−8239

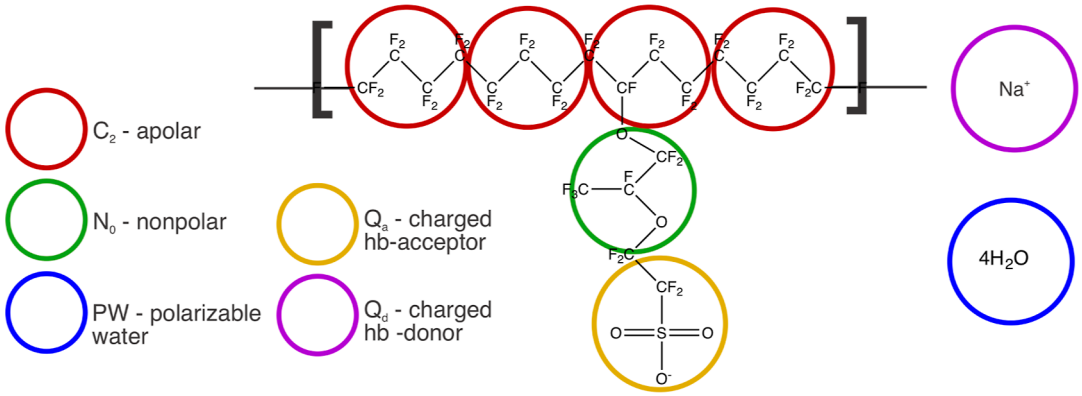

Figure 1. CG mapping of MARTINI beads for one repeat unit of Nafion polymer with EW = 1100 g/mol equiv. Backbone is mapped to four apolar beads (red), side chain is connected to backbone with one nonpolar bead (green), and end of side chain with the sulfonate end group is represented by negatively charged, hydrogen-bond acceptor bead (yellow). Sodium counterions are represented by positively charged hydrogen-bond donor bead (purple). Water beads (blue) each represent contain four molecules of H_2O.

different polymer designs to gain insights into how dispersity and blending affect both the shape of the scattering profile and the real-space morphology of hydrophilic domains.

This work is organized as follows. In Section 2, we describe the CG model, MD simulation protocol, scattering calculations, and real-space structural analyses used in this study. In Section 3, we describe the results of our simulations focusing on how varying ionomer design parameters, including side chain spacing, side chain length, and blending ionomers with different side chain lengths and spacings, affects the resulting self-assembled morphology and scattering. In Section 4, we conclude with implications of our results to experimentalists.

2. METHODS

2.1. Coarse-Grained Model. The CG model used in this work has been adapted from the work by Mabuchi et al.,[53] where the MARTINI v2 force field[47−49] with a polarizable water model[51] was used; their CG model was developed for Nafion with an EW = 1100 g/mol equiv. The CG-mapping of the polymer repeat unit, water, and counterions are shown in Figure 1. The hydrophobic polymer backbone is represented by apolar MARTINI beads of type C_2, and the side chain is composed of a nonpolar MARTINI bead of type N_0, and a charged, hydrogen bond acceptor MARTINI bead Q_a, which represents the sulfonate end group and has a charge of $q = -1e^-$. The positively charged counterion is assigned the charged hydrogen bond donor bead Q_d with charge $q = +1e^-$; at this level of coarse graining, this bead does not distinguish if this is a hydronium ion or Na^+ ion. The water is represented by the polarizable water bead PW, which contains four molecules of water per bead. We refer the reader to the work of Michalowsky et al.[51] for details of the refined polarizable water model.

All the MARTINI beads used in this model have the same diameter of $\sigma = 0.47$ nm. The apolar beads representing the polymer backbone and the nonpolar beads representing part of the side chain each have a mass of 180 amu, the charged bead representing the sulfonate end group has a mass of 200 amu, the polarizable water beads have a mass of 72 amu, and the counterion bead has a mass of 23 amu.

The nonbonded interactions between beads i and j are given as

$$U_{ij}^{\mathrm{nb}} = 4\epsilon_{ij}\left[\left(\frac{\sigma_{ij}}{r_{ij}}\right)^{12} - \left(\frac{\sigma_{ij}}{r_{ij}}\right)^{6}\right] + \frac{q_i q_j}{4\pi\varepsilon_0\varepsilon_r r_{ij}} \tag{1}$$

where r_{ij} is the distance between beads i and j, $q_{i,j}$ is the charge of the bead, ε_r is the relative dielectric constant, which in the refined polarizable water model is set to $\varepsilon_r = 2.5$. ϵ_{ij} is the Lennard-Jones interaction prefactor for beads i and j. The values of ϵ_{ij} are set by the bead types of beads i and j, which are specified by the interaction matrix for the MARTINI v2 force field.[47] The values for ϵ_{ij} for the MARTINI beads used in this work are tabulated in Table S1 in Supporting Information Section S1. The cutoff for both the Lennard-Jones and Coulomb potentials is set to $r_{\mathrm{cut}} = 1.1$ nm, with the potential-shift modifier for the Lennard-Jones potential and the Coulomb potential using reaction-field electrostatics with cutoff dielectric constant set to infinity.

The bonded components of the polymer are connected via a weak harmonic bond potential, which is given by

$$U^{\mathrm{b}} = \frac{1}{2}K_{\mathrm{b}}(r - r_0)^2 \tag{2}$$

where r_0 is the equilibrium bond distance set to $r_0 = \sigma = 0.47$ nm, and K_{b} is the force constant set to $K_{\mathrm{b}} = 1250$ kJ/mol/nm^2. The chain stiffness of the polymer is captured by the harmonic cosine bond angle potential given by

$$U^{\Theta} = \frac{1}{2}K_{\Theta}(\cos(\Theta) - \cos(\Theta_0))^2 \tag{3}$$

where Θ_0 is the equilibrium bond angle and K_Θ is the force constant. The bonds along the chain are connected linearly with an equilibrium bond angle of $\Theta_0 = 180°$, except for the connection between the side chain and the backbone, which has an equilibrium bond angle of $\Theta_0 = 90°$. For more details on the CG MARTINI v2 model and its parameterization, we refer the reader to the manuscript by Mabuchi, Huang, and Tokumasu.[53]

2.2. Simulation Method. We perform MD simulations using the GROMACS 2023 simulation package[55] on high-performance computing clusters. Initial configurations for each simulation are generated using the inset-molecule function of GROMACS, which places each component randomly in the simulation box, and insertions are rejected if the bead's distance with any other existing bead is less than the sum of the van der Waals radii of the two beads or a user-defined cutoff distance. We use a cutoff radius of $r_{\mathrm{insert}} = 0.21$ nm, slightly smaller than the bead radius of $r_{\mathrm{bead}} = 0.235$ nm to allow for some overlaps to ensure that all bead insertions are successful. The polymer structure file is generated using an in-house code to generate CG ionomer chains with grafted side chains according to the prescribed side chain spacing and grafting type (statistical or exact periodic). The initial simulation box size is set to $L_{\mathrm{init}} = 55$ nm. The number of polymer chains (ranging from 500 to 1500) and number of water beads (ranging from 4100 to 135,000) are selected to satisfy initial density $\rho_{\mathrm{init}} = 350$ kg/m^3 and the desired hydration content λ. The ρ_{init} value was chosen to be dilute enough for the inset-molecule function to reliably populate the simulation box. Through the stages described below, we arrive at a final density range of $\rho_{\mathrm{final}} = 1600 - 2500\frac{\mathrm{kg}}{\mathrm{m}^3}$ The number of positively charged counterions are selected to neutralize the charges of all the polymer chains.

https://doi.org/10.1021/acs.macromol.4c00988
Macromolecules 2024, 57, 8223−8239

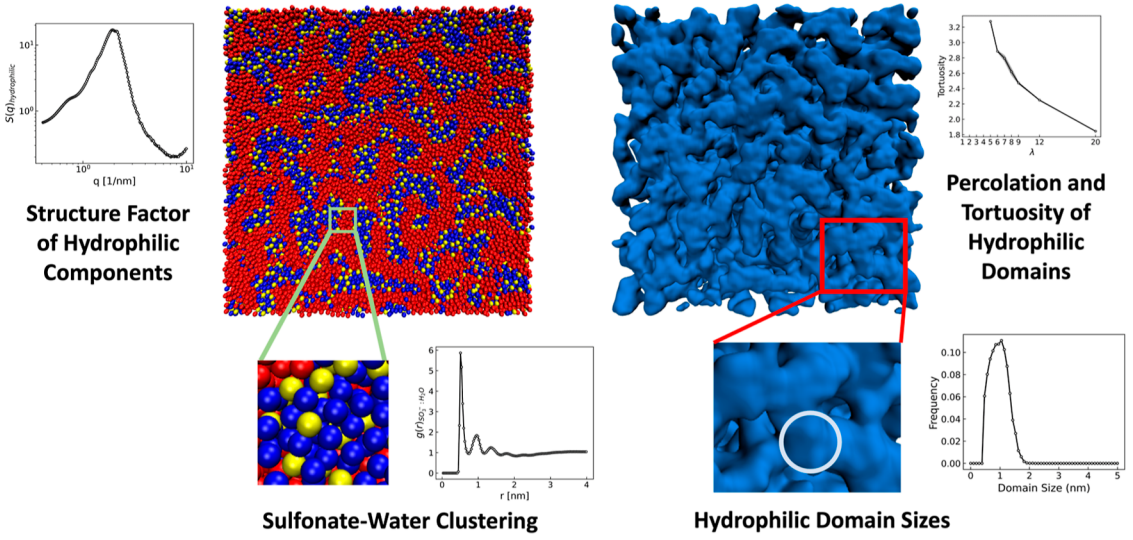

Figure 2. Schematic of the various analyses conducted in this work. From left to right: Structure factors are computed to compare to experimental trends in scattering data. We determine the number of sulfonate−water contacts and radial distribution functions to quantify the changes in the local structures of the hydrophilic domains. We compute the hydrophilic and hydrophobic domain sizes to relate the domain structure to scattering. Lastly, we computed the percolation and tortuosity of the hydrophilic domains to identify promising candidate designs for ion transport.

In the initialization step, we use nonpolar MARTINI beads of the type P_4 in place of the polarizable water beads. This allows us to initialize the simulation without the constrained bonds present in the polarizable water beads because attempting to initialize the simulation with the constrained bonds can cause the LINCS constraint algorithm to fail. When using the nonpolar water beads, the relative dielectric constant is set to the standard value for MARTINI v2, $\varepsilon_r = 15.0$. In this initialization step, the system energy is minimized using the minimization function of GROMACS with the steepest-descent integrator for a maximum of 100,000 time steps. Following energy minimization, an *NVT*-ensemble run is performed with a time step of $dt = 0.001$ ps and a temperature of 600 K using the velocity rescale temperature coupling for 100,000 time steps; by the end of this run, we expect to have removed any bead overlaps. The system is then relaxed away from the selected initial configuration using *NPT*-ensemble simulations and isotropic Berendsen pressure coupling and velocity rescale temperature coupling. We start at $T = 600$ K and $p = 25$ bar for 100,000 time steps, then switch to $T = 600$ K and $p = 50$ bar for 100,000 time steps, and then to $T = 600$ K and $p = 100$ bar. At the end of this routine, we expect the chains to have relaxed away from any unphysical initial configuration. Next, we annealed the system from $T = 600$ K and $p = 100$ bar to the target temperature and pressure. Each stage of this annealing uses 100,000 time steps, with a time step of $dt = 0.01$ ps. The first stage is performed at $T = 500$ K and $p = 75$ bar, the second stage is performed at $T = 400$ K and $p = 50$ bar, and the third stage is performed at $T = 300$ K and $p = 25$ bar. Following this annealing, a simulation run is performed with $dt = 0.01$ ps at $T = 300$ K and $p = 1$ bar for 1,000,000 time steps. By the end of this annealing stage, we expect to have avoided kinetically trapped initial configurations.

After the initialization step, we conduct the actual equilibration at the target temperature and pressure, with polarizability turned on. We switch the nonpolar water beads to polarizable water beads with the dielectric constant changed to the value specified for the polarizable water model, $\varepsilon_r = 2.5$. The system energy is then minimized using the steepest descent integrator for up to 100,000 time steps. Following this, an *NPT*-ensemble run is performed with $dt = 0.01$ ps at the target temperature and pressure, $T = 300$ K and $p = 1$ bar, using the stochastic dynamics integrator for 200,000 time steps, using Berendsen pressure and temperature coupling. The stochastic dynamics integrator and the time step of $dt = 0.01$ ps are used in this step to minimize the chance of the LINCS constraint algorithm failing when we replace the nonpolarizable water beads with the polarizable water beads. Then the molecular dynamics integrator is selected, and an equilibration run of 250,000 with $dt = 0.01$ ps is performed. We monitor the system density and the polymer radius of gyration to ensure that we have achieved equilibrium.

After equilibration, we perform the production stage, which is an *NPT*-ensemble simulation run maintaining $T = 300$ K and $p = 1$ bar using the Berendsen pressure and temperature coupling. In this production run, we use a larger time step of $dt = 0.02$ ps than what we use in equilibration to achieve longer real-time dynamics without any issues with the failing simulations. The entire production run is 10,000,000 time steps, and we collect configurations every 100,000 time steps. The scattering and real-space hydrophilic domain analysis, described in the next section, is performed on 19 configurations collected 500,000 time steps apart. We monitor autocorrelation functions of chain radius of gyration squared and expect the decorrelation time to be ∼500,000 time steps. Further, we run three independent trials for each system to quantify the fluctuations in the analyzed metrics described next, both between trials and within each trial, and confirm that our simulation results are not kinetically trapped and reported error is representative of the largest fluctuations.

2.3. Analysis. Our first goal in this paper is to relate scattering profile features to real-space domain analysis, and to achieve that goal, we perform a variety of structural analyses. Figure 2 summarizes these analysis metrics visually.

2.3.1. Hydrophilic Components' Structure Factors. We compute the structure factor between hydrophilic beads (sulfonate, water, and counterions) using a method based on the work of Brisard and Levitz, which computes the structure factor in reciprocal space while minimizing finite size effects resulting from the cubic shape of the simulation box.[56] The scattering amplitude, $A(q)$, is first computed and normalized by the total number of scatterers

$$A(\boldsymbol{q}) = \frac{\sum_{\mathrm{k}}^{\mathrm{N}} \rho_{\mathrm{k}} \exp(-i\boldsymbol{q}\boldsymbol{x}_{\mathrm{k}})}{N} \tag{4}$$

where ρ_{k} is the scattering length density bead k, N is the total number of simulation beads, and $\boldsymbol{x}_{\mathrm{k}}$ is the position of simulation bead k. Here, we normalize the scattering curve by the number of simulation beads and use $\rho_{\mathrm{k}} = 1$ for the hydrophilic beads and $\rho_{\mathrm{k}} = 0$ for the hydrophobic beads because we wish to quantify the shape of the hydrophilic components' scattering profile. This choice of scattering length densities provides the scattering contrast between hydrophilic and hydrophobic domains but is not directly analogous to scattering experiments, where each chemical species would have its own scattering length density. We also perform the structure factor calculation for a subset of the simulations using scattering length densities based on

https://doi.org/10.1021/acs.macromol.4c00988
Macromolecules 2024, 57, 8223−8239

previous experimental work. We find that by using these experimentally informed scattering length densities, the ionomer peak q-value remains the same as that seen when we use $\rho_k = 1$ for the hydrophilic beads and $\rho_k = 0$ for the hydrophobic beads. We also find matching qualitative trends in the low-q scattering intensity and ionomer peak intensity for the two choices of scattering length densities. Related discussion can be found in the Supporting Information Section SII. The benefit of using $\rho_k = 1$ for the hydrophilic beads and $\rho_k = 0$ for the hydrophobic beads lies primarily in that the calculation is significantly faster as the summation only occurs over a minority subset of the simulation beads, rather than the summation being over every simulation bead in the case where each bead's scattering length density needs to be considered.

The form factor of the cubic box is subtracted from the scattering amplitude, yielding the scattering amplitude free of finite box-size effects, $A_{bs}(\boldsymbol{q})$

$$A_{bs}(\boldsymbol{q}) = A(\boldsymbol{q}) - \prod_{i=x,y,z} \frac{\sin\left(\frac{q_i}{L}\right)}{\left(\frac{q_i}{L}\right)} \tag{5}$$

Then, the structure factor is computed as follows

$$S(q) = \sum_{k}^{N} \rho_k \overline{|A_{bs}(\boldsymbol{q})|^2} \tag{6}$$

where the overbar represents averaging over all orientations of the wavevector $\boldsymbol{q}$. In our calculation, for each magnitude, q, of the $\boldsymbol{q}$ wavevector, we sampled 500 orientations using a Fibonacci sphere to ensure roughly even sampling across orientations. The q-range used for the structure factor ranges from $q_{min} = \frac{2\pi}{L}$, where L is the simulation box length, to $q_{max} \cong 7\ nm^{-1}$, which is chosen as a q-value below the range where the structure factor is influenced by the radius and packing of the simulation beads.

As noted in the previous section, we calculate the structure factor for 19 configurations for each trial, starting at t = 1,000,000 time steps and spaced out every 500,000 time steps. We report the mean of the three trials' structure factors and the standard error of the three curves.

2.3.2. Hydrophilic and Hydrophobic Real-Space Domain Sizes, Tortuosity, and Connectivity. We quantify the changes in the size and connectivity of hydrophilic domains (consisting of sulfonate groups, water, and sodium counterions) by determining whether the domains percolate the simulation box in each of the x, y, and z directions, by calculating the overall tortuosity of the hydrophilic domains and by calculating the hydrophilic domain size distribution. We also quantify sizes of the hydrophobic domains consisting of polymer backbone beads (BBs) and uncharged side chain beads.

To determine the percolation in hydrophilic domains of the structure, a graph is constructed first. In this graph, all nodes represent the water, sulfonate, and counterion simulation beads, and edges connect those nodes that are closer than a certain cutoff distance. A subgraph is constructed from each connected component of the original graph, and a check is performed on each subgraph to determine whether the subgraph spans the simulation box in the x, y, and z directions. In our results, we quantify the percolation by describing the number of directions in which the hydrophilic domains are percolated, ranging from 0 (not percolated in any direction) to 3 (percolated in each of the x, y, and z directions). This implementation is done using Python's NetworkX module.[57]

To quantify the tortuosity of hydrophilic channels through the structure, we use Python's PoreSpy implementation of tortuosity.[58] First, we convert our simulation snapshot to a voxelized representation, where each voxel takes the identity of the nearest simulation bead. We then binarize the voxel representation, with sulfonate, water, and ion voxels taking the value 1 and polymer backbone and side chain voxels taking the value 0. The binary voxel representation is passed to PoreSpy's tortuosity_fd function, which computes the tortuosity of the hydrophilic domains. Specifically, the tortuosity is computed as the ratio between the diffusivity calculated from the structure of interest and the diffusivity calculated for a structure consisting of only one phase, where both diffusivities are calculated by using finite difference simulations based on continuum diffusion equations. As such, values can range from 1 (perfectly straight channels, where the diffusivity in a given direction will be equivalent to that in a bulk liquid) to arbitrarily high values (for very tortuous paths, where the diffusivity is much larger than in the bulk medium). It should be noted that this computation is purely based on the geometry of the paths resulting from the hydrophilic domain structure and does not consider specific chemical information, such as the positions of sulfonate ions and their interactions with water, cations, and counterions, that would also affect the diffusivity of these species.

We compute the distribution of hydrophilic domain sizes using a method inspired by the determination of pore sizes in DNA cross-linked hydrogels by Wang et al. and in porous silica by Bhattacharya and Gubbins.[59,60] For each analyzed simulation snapshot, we randomly sample 1000 points within the simulation box and define the domain size for each sampled point as the diameter of the largest sphere that encompasses the sampled point and does not overlap with the surrounding polymer backbone or side chain beads. For the hydrophobic domain sizes, the same procedure is used; the domain size for each sampled point is the diameter of the largest sphere that does not overlap with surrounding sulfonate, water, or cation beads. We used the hydrophobic domain sizes to quantify the spacing between the hydrophilic domains.

The real-space domain size distributions, connectivity, and tortuosity calculations are performed on 19 configurations for each of the three trials performed, starting at t = 1,000,000 time steps, at every 500,000 time steps. The results for all the 57 configurations (i.e., 3 trials × 19 configurations/trial) are pooled together to determine the ensemble average and standard error.

2.3.3. Sulfonate–Water Bead Coordination Number. We calculate the number of water beads that are within the chosen cutoff distance of r_{cut} = 0.6 nm to each sulfonate bead to characterize the local environment around the sulfonate beads in terms of whether the nearest neighbors are water beads. This analysis is done to understand some of the molecular-level underpinnings of the domain-level structural analyses described above. These calculations are performed on 19 configurations for each of the three trials performed starting at t = 1,000,000 time steps, at every 500,000 time steps. We report the mean of the pooled 57 configurations.

2.4. Parameters Varied. Besides relating structure factor features to real-space domain analysis, one of our other goals in this paper is to understand how dispersity in ionomer designs affects the hydrophilic domain structure. To achieve these goals, we need to systematically vary the ionomer designs to establish the baseline (isolated) effect of each ionomer design parameter (side-chain length and spacing) before considering the dispersity or blending effect. To accomplish that, we vary the number of BBs between side chains denoted as the side chain spacing Γ_{sc} and vary the number of beads in the side chain denoted as the side chain length $l_{sc} = 2$ (Figure 3). When varying either the side chain spacing or the side chain length, the other parameter is held to the value established for Nafion (EW = 1100g/mol equiv)—$\Gamma_{sc} = 4$ and $l_{sc} = 2$, respectively. It is worth noting that changing the side chain length inherently changes the ratio of SO_3^- to inactive sites (SC and BB); as a result, changes to side chain length inherently vary the EW.

The side chain spacing Γ_{sc} relates to the **EW** of the polymer; our simulated values of side chain spacing Γ_{sc} = 2, 4, and 8, with $l_{sc} = 2$, correspond to 740, 1100, and 1820 in EW (Table 1). It is recognized that neither 740 EW nor 1820 EW membranes are currently commercially manufactured; however, the current work is intended to develop general design rules for hydrated ionomer morphology.

The side chain length l_{sc} is varied by adding or removing the nonpolar MARTINI beads (N_0) that makes up the uncharged components of the side chain. In the case of $l_{sc} = 1$, the charged side chain bead is connected directly to the backbone. The values of side chain length l_{sc} considered in this study are 1–3 with $\Gamma_{sc} = 4$. The EWs for chains with $\Gamma_{sc} = 4$ and $l_{sc} = 1$, 2, 3 are 920, 1100, and 1300, respectively (Table 1). It is important to note that variations in the EW, especially in the range of 720–1100, are known to cause significant

https://doi.org/10.1021/acs.macromol.4c00988
Macromolecules 2024, 57, 8223–8239

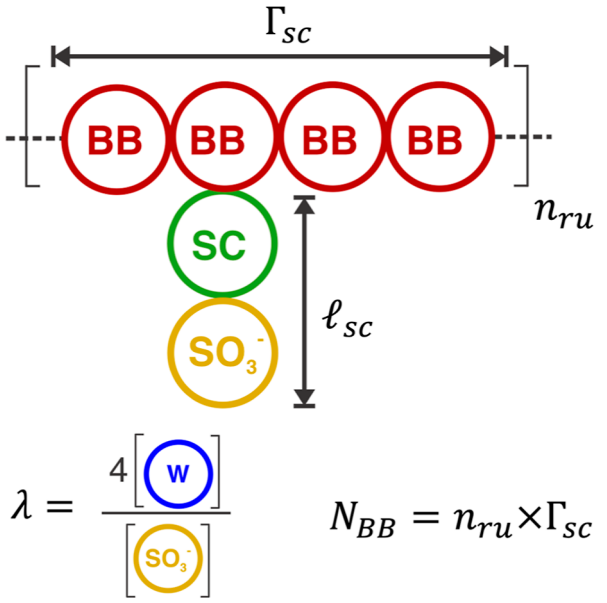

Figure 3. Side chain spacing, Γ_{sc}, corresponds to the number of backbone beads (BBs) between side chains. The side chain length, l_{sc}, corresponds to the number of MARTINI beads that comprise the grafted side chain. The number of BBs, N_{BB} in a chain is set by the number of repeat units n_{ru} and Γ_{sc}. The water content is set by λ, which is the number of water molecules per sulfonate end group present in the system.

Table 1. EW of Simulated Ionomers for Given Side Chain Spacing (Γ_{sc}) and Side Chain Length (l_{sc})

equivalent weight (EW) (g/mol)		Γ_{sc}		
		2	4	8
l_{sc}	1	560	920	1640
	2	740	1100	1820
	3	920	1280	2000

differences in the ionomer microstructure and performance in experiments.[61]

The number of BBs per chain is set by $N_{bb} = n_{ru} \times \Gamma_{sc}$, where n_{ru} is the number of repeat units. When varying the side chain spacing and the side chain lengths, the number of BBs per chain is held constant at or near $N_{bb} = 100$. We also vary the extent of hydration characterized by the ratio of the number of water molecules to the number of sulfonate end groups, $\lambda = [H_2O]/[SO_3^-]$.

First, we evaluate the effects of changing the side chain spacing Γ_{sc} and the side chain length l_{sc} when all chains have the same chain length, Γ_{sc} and l_{sc} (i.e., monodisperse systems). Each monodisperse system is simulated with varying hydration contents, $\lambda = 1-20$.

Next, we consider the dispersity effects by studying the following three cases:

(i) Binary mixtures of precise, periodic side chain spacings (Figure 4): in the binary mixtures of precise, periodic side chain spacings, the lower-value side chain spacing is designated Γ_{sc}^{A}, and the higher-value side chain spacing is designated Γ_{sc}^{B}.

(ii) Binary mixtures of side chain lengths: in binary mixtures of side chain lengths, the lower-value side chain length is designated l_{sc}^{A}, and the higher-value side chain length is designated l_{sc}^{B}.

In all binary mixtures, the proportions of chain A and chain B are set according to the fraction of chain A, f_A.

(iii) Polydisperse systems of statistical side chain spacings, with predetermined side chain spacing mean and standard deviations (Figure 5): in the polydisperse system of statistical side chain spacings, each chain has a unique set of side chain spacings along the chain selected from a Gaussian distribution with a predetermined mean $\langle\Gamma_{sc}\rangle$ and standard deviation $\sigma_{\Gamma sc}$. The number of repeat units are held constant, and chains with number of BBs greater than $N_{bb} = n_{ru} \times \langle\Gamma_{sc}\rangle$ and less than $N_{BB} = (n_{ru} - 1) \times \langle\Gamma_{sc}\rangle$ are rejected.

Lastly, in Supporting Information Section SIII, for a select few systems ($\Gamma_{sc} = 4$, $l_{sc} = 2$, and $N_{bb} = 100$), we compare the results from simulations using polarizable water model against analogous simulations using a nonpolarizable water model. This shows the reader the explicit impact of using the polarizable water model in this work.

3. RESULTS AND DISCUSSION

In the following subsections, we start by first comparing the various analysis metrics for monodisperse systems at varying hydration. While previous simulation studies have elucidated many of these effects of ionomer design on structure for monodisperse systems, we simulate such a monodisperse system for two reasons: one, our results showing the effects of these seemingly simple design variations in monodisperse systems support our argument that there is a nontrivial link between features of the scattering profiles and real-space domain analyses, and two, having the monodisperse system results

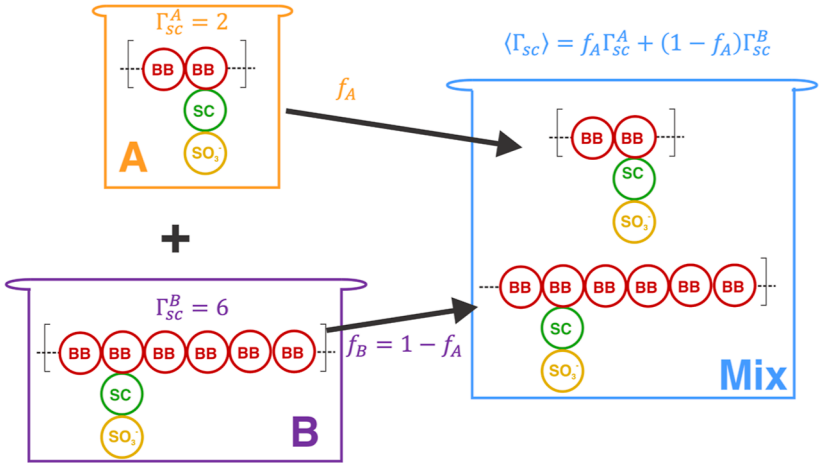

Figure 4. Schematic showing the binary blends of ionomers with different side chain spacings Γ_A and Γ_B. The proportions of each ionomer in the solution are set by the chain fractions of each component f_A and f_B to achieve the desired solution-averaged side chain spacing $\langle\Gamma_{sc}\rangle$.

https://doi.org/10.1021/acs.macromol.4c00988
Macromolecules 2024, 57, 8223−8239

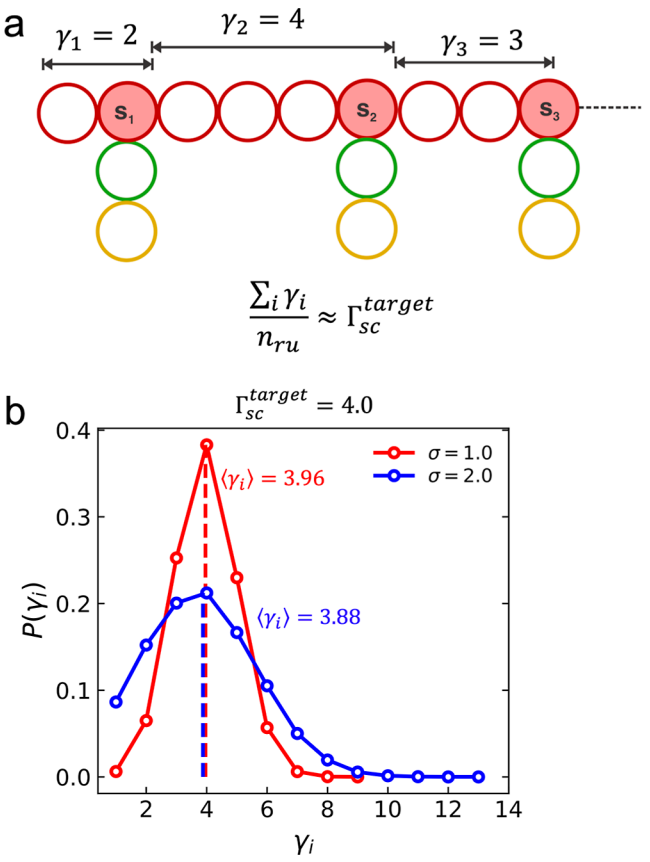

Figure 5. Schematic showing the statistical side chain spacing chains (a). The spacings between each side chain are chosen from a pseudo-Gaussian distribution that is set by the target mean spacing $\langle\gamma_i\rangle$ and the standard deviation σ (b).

establishes a baseline for comparison with results we report for our novel blends and polydisperse systems.

3.1. Effects of Varying Hydration on Structure Factors and Real-Space Structural Features. We establish the baseline morphology of Nafion with EW = 1100 at varying extents of hydration, $\lambda = 1$ to $\lambda = 20$, and side chain spacing $\Gamma_{sc} = 4$ and side chain length $l_{sc} = 2$.

Bulk morphology is characterized by measuring the partial structure factor of the hydrophilic components, which corresponds to typical scattering measurements of hydrated ionomers. Figure 6a shows the partial structure factor of the hydrophilic components (the bottom x-axis shows the q values, and the top x-axis shows the corresponding real length scales). While past studies only focus on the ionomer peak in the scattering profile, we connect the ionomer peak location, breadth, and intensity, as well as the intensity at the low q-range, to the observed morphologies in real space. Figure 6a shows that as the extent of hydration is increased (red to blue), the scattering peak location shifts toward lower q-values, which corresponds to shifts toward larger real-space distances. The peak intensity does not vary considerably as the extent of hydration is increased. There is a strong effect on the scattering intensity in the low-q range (0.4−0.7 nm^{-1}) where the intensity increases monotonically as the hydration content increases. For $\lambda = 4$, there is a substantial increase of the low-q scattering intensity that begins to approach the value of the ionomer peak scattering intensity. The trends in the shifts observed in the scattering profiles are similar to the results presented by Sorte et al.,[62] where they performed atomistic simulations and experiments to study the effects of hydration content and sulfonation on Diers−Alders poly(phenylene) membranes. Sorte et al. observed increases in the scattering peak intensity and a peak shift toward lower q-values with increased hydration in the water partial structure factor.

To understand the implications of changing features of the scattering profiles as hydration is varied, we performed a real-space analysis on the hydrophilic domain structures. Figure 6b shows the size distributions of the hydrophilic domains at various λ. As λ is increased (red to blue), the mean domain size shifts toward larger length scales. The hydrophilic domain size distributions at low hydration of $\lambda \leq 3$ show a narrow, approximately symmetric distribution that widens slightly with increased hydration. At higher hydration, $\lambda = 6$, the distributions become significantly broader and show a shift from a symmetric distribution to a more skewed distribution. Beyond the mean size of the distribution at higher λ, the distribution decays more rapidly than in the range preceding the peak, before reaching a "tail"—feature where the distribution decays much more slowly, showing the presence of few, large hydrophilic domains. The features of the hydrophilic domain size distributions that show significant changes with varying hydration contents include the mean domain size, the width of the domain size distribution, and the skewness and tail of the distribution. As the hydrophilic domain sizes and the spacing between the hydrophilic domains due to the presence of hydrophobic domains will impact the scattering peak location, we calculate the domain sizes of the hydrophobic domains. The hydrophobic domain sizes (i.e., spacing between hydrophilic domains) only slightly decrease with increasing hydration (Figure 6b, inset). As such, it makes sense that the ionomer peak shifts to lower q-values as the hydrophilic domain sizes increase, while the spacing between them remains relatively constant. The hydrophilic domain size distributions show a significant change to the tail of the distribution as the extent of hydration is increased from $\lambda = 12$ to $\lambda = 20$; similarly, there is a significant change to the scattering intensity at the low q-range, $\lambda = 12$ to $\lambda = 20$. The increase in the scattering intensity in the low q-range is likely due to the formation of significantly larger hydrophilic domains, as the tail of the domain size distributions shows.

In addition to the hydrophilic domain size distributions, the connectivity and shapes of the hydrophilic domains are characterized by analyzing the percolation of the hydrophilic domains and the tortuosity of the percolated hydrophilic domains. Tortuosity and percolation of the hydrophilic domains have a significant impact on the proton transport properties[63−65] and are substantially impacted by the hydration content as shown in Figure 6c,d. Figure 6c shows the results of the percolation analysis, which describes the average number of cardinal directions the hydrophilic domains are percolated in as a function of the hydration content λ. The hydrophilic domains remain completely unpercolated as the hydration content increases from $\lambda = 1$ to $\lambda = 4$. Starting at $\lambda = 5$, the domains begin to show partial percolation. Beyond $\lambda = 5$, there is an increase in the number of directions percolated with increased hydration, and full percolation is reached at $\lambda = 12$. Figure 6d shows the tortuosity of the percolated hydrophilic domains as a function of λ, where the tortuosity decreases with increasing λ, and the rate of decrease gradually lowers beyond $\lambda = 9$, which corresponds to the domains becoming fully percolated.

The average coordination number between the sulfonate beads and water is calculated as a function of hydration content λ

https://doi.org/10.1021/acs.macromol.4c00988
Macromolecules 2024, 57, 8223−8239

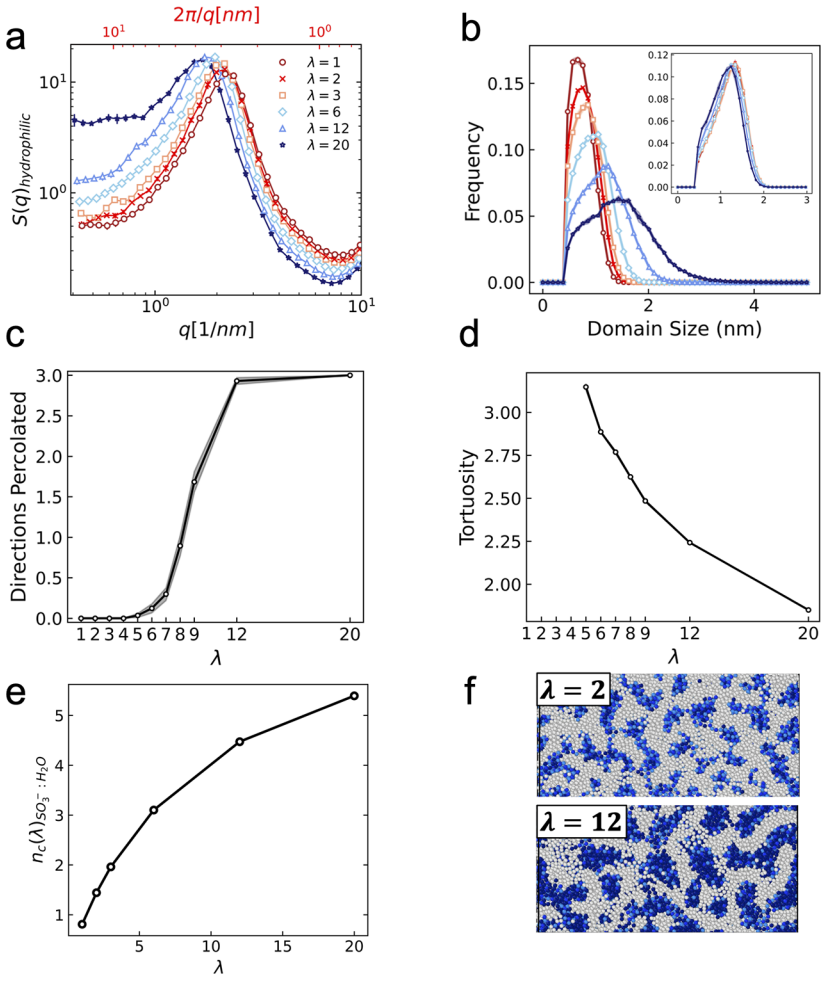

Figure 6. Structural analyses for ionomers with side chain spacing $\Gamma_{sc} = 4$ and side chain length $l_{sc} = 2$. (a) Partial structure factor of the hydrophilic components (water, sulfonate, and counterion beads) at various extents of hydration λ. (b) Hydrophilic domain size distributions at various λ. The inset of (b) shows the hydrophobic domain size distributions with changing hydration. (c) Hydrophilic domain directions percolated vs λ. (d) Tortuosity of percolated hydrophilic vs λ. (e) Average number of water bead contacts per sulfonate bead vs λ. (f) Simulation snapshots at $\lambda = 2$ (top) and $\lambda = 12$ (bottom), with hydrophobic components in white and hydrophilic components in blue.

and is shown in Figure 6e. The number of contacts between the sulfonate beads and water increases as the hydration content is increased, where the rate of increase declines with increasing λ. From these calculations, it is clear that as the water concentration is increased and the hydrophilic domains become larger, the sulfonate beads interact with more water beads. This increase in the coordination number with increased λ implies a shift in the local environment around the sulfonate beads, which can be observed in the simulation snapshots shown in Figure 6f. The relationship between the number of contacts between water and sulfonates and the mean domain size is shown in Figure S1 in the Supporting Information. There is initially a linear relationship between the number of water and sulfonate contacts and the mean hydrophilic domain size at lower hydration, and once a certain hydration content is reached, the growth in the mean domain size outpaces the increase in the number of water and sulfonate contacts. The point at which the mean domain size growth outpaces the increase in water−sulfonate contacts and the extent of this increased domain size growth are dependent on the design parameters, Γ_{sc} and l_{sc}, chosen.

Figure 6f shows snapshots of the simulation box for $\lambda = 2$ (top) and $\lambda = 12$ (bottom), where the hydrophobic components (polymer backbone and uncharged side chain beads) are shown in white and the hydrophilic components are shown in shades of blue, with the sulfonate beads shown in light blue and the water beads in dark blue. In both the low hydration and high hydration snapshots, the hydrophilic components form domains that have a worm-like anisotropic shape. At low hydration, the hydrophilic domain thickness is significantly smaller than that at high hydration, which leads to the sulfonate beads having more contacts with the hydrophobic components. The domain shapes and organization of the sulfonate beads and water beads lead to the lower coordination number between sulfonate bead and water beads at low hydration. As the hydrophilic domains grow in thickness with increasing water, the water and sulfonate beads gain the ability to organize such that there are more contacts between water and sulfonate beads and less contact between sulfonate beads and the hydrophobic components (Figure S2 in the Supporting Information), which in turn leads to a decrease in the tortuosity of the hydrophilic domains.

We have established the relationship between hydration content and the morphology of the hydrophilic domains, as characterized by our scattering measurements and real-space domain analysis, for the ionomer design based on Nafion with EW = 1100. The percolation analysis revealed an onset of percolation starting around $\lambda = 5$ and full percolation (i.e., all 3

https://doi.org/10.1021/acs.macromol.4c00988
Macromolecules 2024, 57, 8223−8239

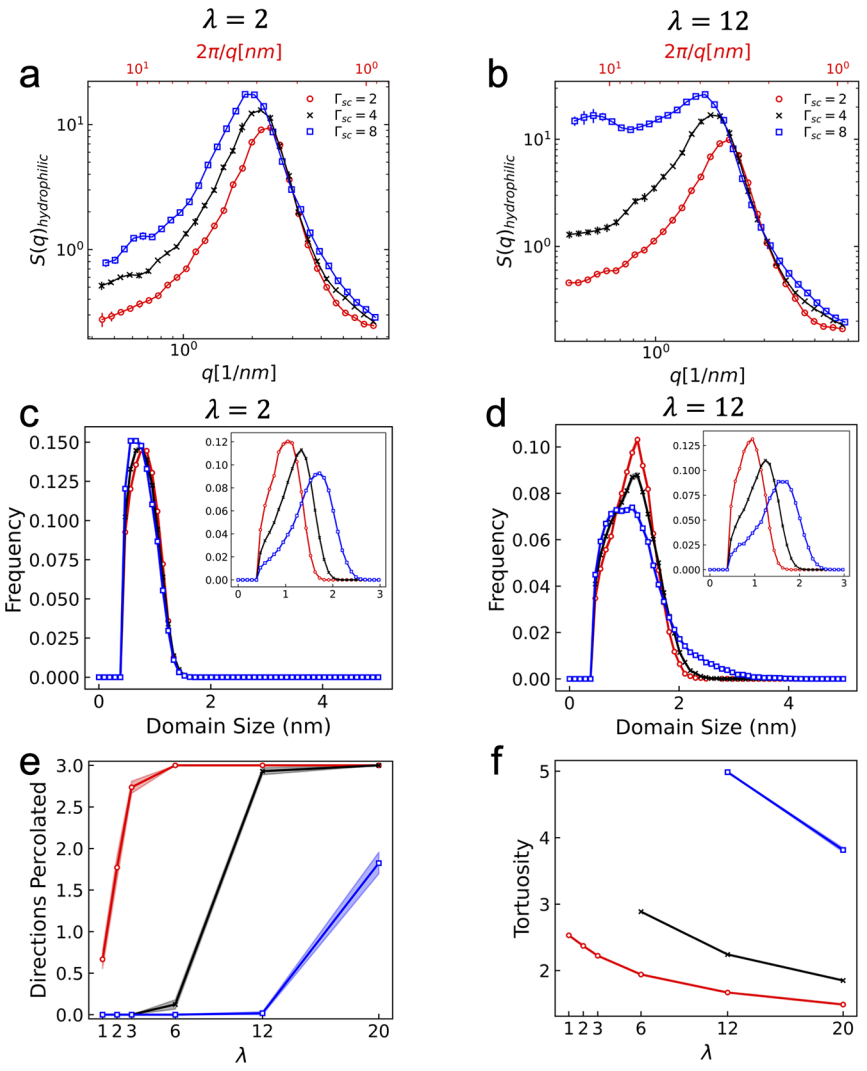

Figure 7. Structural analyses for monodisperse systems with varying side chain spacing Γ_{sc} and side chain length $l_{sc} = 2$. Partial structure factor of the hydrophilic components (water, sulfonate, and counterion beads) at $\lambda = 2$ (a) and $\lambda = 12$ (b). Hydrophilic domain size distributions were obtained for $\lambda = 2$ (c) and $\lambda = 12$ (d). Insets in (c) and (d) show the hydrophobic domain size distributions. (e) Plot of the hydrophilic domain directions percolated vs λ. (f) Plot of tortuosity of percolated hydrophilic vs λ.

dimensions) at $\lambda = 12$, and the tortuosity measurements show a decrease in tortuosity with increased λ. The hydrophilic domain size distributions show a shift toward larger domain thicknesses and broader distributions with increased λ, and the hydrophobic domain size distributions remain the same with increasing λ. Understanding how these changes in morphology manifest in the scattering profile is a crucial insight necessary for optimizing ionomer design as scattering measurements remain the most accessible and utilized characterization method for hydrated ionomers.

Next, we do the scattering and real-space analysis for ionomers with varying side chain spacings and side chain lengths to understand the relationship between the real-space morphological features and the features observed in the scattering profiles.

3.2. Varying Side Chain Spacing−Monodisperse System vs Blended/Polydisperse Systems. *3.2.1. Monodisperse Systems.* Simulations are performed on ionomers of varying side chain spacings to understand its impact on structure. The metric Γ_{sc} is used to denote the number of BBs between each side chain. A crucial implication of varying the side chain spacing is the change in the overall water concentration for a given value of λ. We choose to maintain the same values for λ for the different designs as this is the primary way the water content is characterized in studies of ionomers. This chosen method will result in the volume fraction of water changing with varying side chain spacing (or EW) and should be taken into consideration when reviewing the results. Additionally, we choose to maintain consistent chain lengths across the different designs by varying the number of repeat units accordingly between the different side chain spacings. The effects of chain length and number of repeat units on the hydrated morphology become negligible with sufficiently large chains (Figures S3 and S4 in Supporting Information).

The scattering profiles for the three side chain spacings modeled are shown for low hydration, $\lambda = 2$ (Figure 7a), and for high hydration, $\lambda = 12$ (Figure 7b). At low hydration, the scattering peak location shifts toward lower q-values, and the scattering peak intensity increases as the side chain spacing is increased. Increasing the side chain spacing while maintaining the same λ-value results in a decrease in the overall water concentration. In the previous section, when λ was varied for the

https://doi.org/10.1021/acs.macromol.4c00988
Macromolecules 2024, 57, 8223−8239

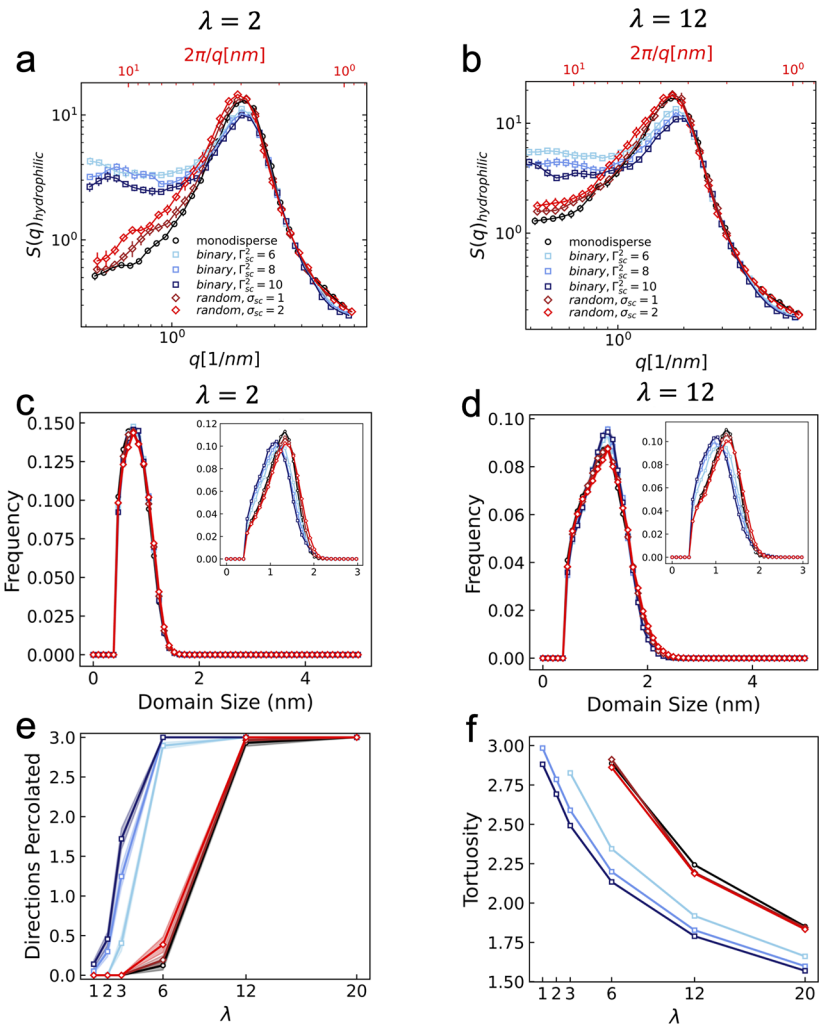

Figure 8. Results for ionomers with average side chain spacing $\langle\Gamma_{sc}\rangle = 4$ including monomodal solution (black), binary mixtures (blue), and mixtures with statistical side chain spacing (red). The three binary mixtures are made up of the following side chain spacings, $\Gamma_{sc}^{A} = 2$, 2, and 2 and $\Gamma_{sc}^{B} = 6$, 8, and 10, with fractions of chain A, $f_A = 0.5$, 0.66, and 0.75. Partial structure factor of the hydrophilic components (water, sulfonate, and counterion beads) at $\lambda = 2$ (a) and $\lambda = 12$ (b). Hydrophilic domain size distributions for $\lambda = 2$ (c) and $\lambda = 12$ (d). Insets in (c) and (d) show the hydrophobic domain size distributions. (e) Plot of the hydrophilic domain directions percolated vs λ. (f) Plot of tortuosity of percolated hydrophilic vs λ.

same ionomer design, the growth in hydrophilic domain sizes coincided with an increase in the water concentration and a shift to lower q of the scattering peak. Here, we still see significant shifts in the scattering profiles, despite the similar hydrophilic domain size distributions at low hydration between the three values of side chain spacings (Figure 7c). There is a slight shift toward smaller mean hydrophilic domain size with increased Γ_{sc}, but the spacing between these hydrophilic domains increases significantly as side chain length increases (Figure 7c, inset). In this case, the shift of the ionomer peak to lower q is caused by increase spacing between the hydrophilic domains (i.e., hydrophobic domain sizes) rather than the increase in the hydrophilic domain sizes themselves.

At high hydration (Figure 7b), we observe similar trends in the scattering profile as in the low hydration case. There is a shift in the peak location toward smaller q-values and a slight increase in the peak intensity with increasing Γ_{sc}. At high hydration, we observe a more substantial increase in the scattering intensity in the low-q range than in the low-q case, particularly as the spacing is increased from $\Gamma_{sc} = 4$ to $\Gamma_{sc} = 8$, with the low-q scattering intensity at $\Gamma_{sc} = 8$ approaching that of the peak intensity. In Figure 7d, we observe similar hydrophilic domain size distributions for $\Gamma_{sc} = 2$ and $\Gamma_{sc} = 4$, with the distribution broadening with increasing Γ_{sc}. The hydrophilic domain size distribution at $\Gamma_{sc} = 8$ at high hydration has a different profile than in the other two side chain spacings; it shows a significantly broader peak with a persistent tail that extends out toward a domain size of 4 nm. The hydrophilic domain size distribution for $\Gamma_{sc} = 8$ shows the formation of significantly larger hydrophilic domains, which is reflected in the increased low-q scattering intensity. The spacing between the hydrophilic domains due to the presence of hydrophobic domains is not significantly affected by the level of hydration as similar distributions of the hydrophobic domain sizes are seen at $\lambda = 12$ as compared to $\lambda = 2$. It is apparent that in the case of $\Gamma_{sc} = 8$, the difference in the scattering profile, particularly the increase in low-q scattering, is a result of the hydrophilic domains growing significantly while maintaining similar hydrophobic domain size and therefore hydrophilic domain spacing as in the low hydration case.

In Figure 7e, the onset of percolation changes significantly with varying Γ_{sc}; the onset of percolation is at low hydration ($\lambda = 1$) for $\Gamma_{sc} = 2$ and at high hydration ($\lambda = 20$) for $\Gamma_{sc} = 8$. The tortuosity of the percolated hydrophilic domains increases with increasing Γ_{sc}. A high side chain spacing leads to larger, less

https://doi.org/10.1021/acs.macromol.4c00988
Macromolecules 2024, 57, 8223−8239

connected, and more tortuous hydrophilic domains (Figures 7 and S5 in Supporting Information). A low side chain spacing will produce hydrophilic domains that are percolated even at low hydration and have low tortuosity while maintaining a similar domain thickness to the domains in $\Gamma_{sc} = 4$ (Figures 7 and S5 in Supporting Information). As we know that increasing the side chain length while maintaining constant λ leads to a decrease in the system water volume fraction, we plot the percolation and tortuosity analysis for the varying side chain lengths against the system water volume fraction in Figure S6 in Supporting Information, where the same trends are observed as in Figure 7e,f.

With changing side chain spacing, the shifts observed in the scattering peak and location at both low and high hydration are driven by the changes in spacing between the hydrophilic domains, rather than the size of the domains. Additionally, the formation of large hydrophilic domains in the case of $\Gamma_{sc} = 8$ at high hydration is reflected in the low-q scattering intensity. The shifts in the scattering peak location with increased side chain spacing are similar to results from the study by Win et al.,[66] where they studied the effects of varying the degree of sulfonation of fluorine-free terpolymers on the hydrophilic and hydrophobic domain structure. By increasing the degree of sulfonation, the ion exchange capacity of the polymer is increased, similar to decreasing the side chain spacing in our study. Win et al. observed a shift toward higher-q values of the ionomer peak and a decrease in the low-q scattering intensity with increased sulfonation.

3.2.2. Blends of Chains with Different Side Chain Spacing and Polydisperse Systems with Varying Side Chain Spacing within Each Chain. In the case of binary blends, we consider two populations of ionomer chains with side chain spacing values Γ_{sc}^{A} and Γ_{sc}^{B}; fraction of chain A, f_A, is set to result in a prescribed mean side chain spacing value of $\langle\Gamma_{sc}\rangle = 4$. The three binary blends have $\Gamma_{sc}^{A} = 2$, 2, and 2; $\Gamma_{sc}^{B} = 6$, 8, and 10; and $f_A = 0.5$, 0.66, and 0.75. In the case of polydisperse systems, ionomer chains' side chain spacing values were selected from a Gaussian distribution (as detailed in Section 2.4) with $\langle\Gamma_{sc}\rangle = 4$, and varying standard deviations, $\sigma_{sc} = 1,2$. The spacing distributions and mean spacing values are shown in Figure 5b. These five mixed (blends or polydisperse) systems are compared to the one monodisperse system with an exact periodic spacing of $\Gamma_{sc} = 4$. All systems have $l_{sc} = 2$.

Plots of the partial structure factor of the hydrophilic components at low and high hydration (Figure 8a,b) show two distinct profiles distinguished between the three binary blends (blue), the two polydisperse (red), and monodisperse systems (black). At low hydration, the binary blends have a slightly lower scattering peak intensity and higher scattering intensity at the low-q range than the polydisperse and monodisperse systems. Among the binary blends, the low-q scattering intensity increases as the magnitude of the difference between the spacing of chain A and chain B, $|\Gamma_{sc}^{A} - \Gamma_{sc}^{B}|$, is decreased. Between the monodisperse and polydisperse, the former shows lower scattering intensity in the low-q range, and the latter shows that the spacings selected from the broader distribution, $\sigma = 2$, lead to higher scattering intensity at the low-q range. At high hydration, the same trends in the scattering profiles observed at low hydration follow, with all systems showing higher low-q scattering intensities as compared to the low hydration state.

The hydrophilic domain size distributions at low hydration (Figure 8c), show no difference between the six systems. At high hydration (Figure 8d), the hydrophilic domain size distributions vary only slightly in breadth, with the binary blends having a narrower distribution and the polydisperse system having a broader size distribution with the monodisperse system's behavior lying in between the two—binary blend and polydisperse. In the three binary blends, the side chain spacings for chain A are all set to $\Gamma_{sc} = 2$. At high hydration, the presence of chains with a small side chain spacing appears to have an impact on the resulting hydrophilic domains, with the side chain spacing of chain B having a smaller impact on the morphology. Increasing the variance of the side chain spacings along the chains in the polydisperse system leads to broader hydrophilic domain size distribution. Again, the hydrophobic domain sizes that create the spacing between the hydrophilic domains are more significantly affected by varying the design of the ionomer blend. At both low and high hydration, the binary blends have hydrophilic domains that are slightly closer together than those of the monodisperse and random polydisperse systems. As the side chain spacing of the second component in the binary blend increases, the spacing between the hydrophilic domains decreases. Meanwhile, as σ_{sc} increases for the random dispersity systems, the hydrophobic domain size distributions become broader. As with the monodisperse systems with varying side chain spacing, the shift in ionomer peak location is primarily explained by the spacing between the hydrophilic domains rather than the hydrophilic domain size.

Interestingly, in line with the scattering profile trends and hydrophobic domain size distributions, the propensity for percolation and the tortuosity of the percolated hydrophilic domains for the binary blends are distinct from those of the monodisperse and polydisperse systems. Figure 8e shows that the binary blends have an onset of percolation that occurs between $\lambda = 1$ and $\lambda = 3$. The onset of percolation between the binary blends correlates with the magnitude of the difference between the spacing of chains A and B, $|\Gamma_{sc}^{A} - \Gamma_{sc}^{B}|$, where an increase in the difference leads to the onset of percolation at a lower value of λ. In the preceding section, we observed that the low side chain spacing, $\Gamma_{sc} = 2$, is partially percolated at $\lambda = 1$. The binary blends contain some number of chains with $\Gamma_{sc} = 2$, and their propensity to percolate at lower λ correlates with the fraction of chain A, f_A, with $\Gamma_{sc} = 2$. Similarly, the tortuosity vs λ (Figure 8f) shows the same trend where having more chains with $\Gamma_{sc} = 2$ leads to domains with lower tortuosity. For both the onset of percolation and the tortuosity of the percolated domains, the monodisperse system behaves similarly to the polydisperse system, with no perceptible difference between the two polydisperse systems with different σ_{sc}.

Overall, polydispersity in the side chain spacing along each chain does not bring about a different behavior compared to a monodisperse system with the same average side chain spacing. However, creating binary blends with the same average side chain spacing as the monodisperse system shows substantially different percolation behavior and tortuosity; this is due to the presence of chains with a low side chain spacing having a strong influence on the percolation and tortuosity as well as shifts toward smaller hydrophilic domain spacing as compared to the monodispersed and random grafted systems.

As to why the binary blends show an increase in the low-q scattering intensity as compared to the monodisperse and polydisperse systems is not obvious as the spacing between hydrophilic domains is lower for the binary blend systems despite showing higher low-q scattering intensity. If we consider the monodisperse systems, chains with $\Gamma_{sc} = 8$ show a large

https://doi.org/10.1021/acs.macromol.4c00988
Macromolecules 2024, 57, 8223−8239

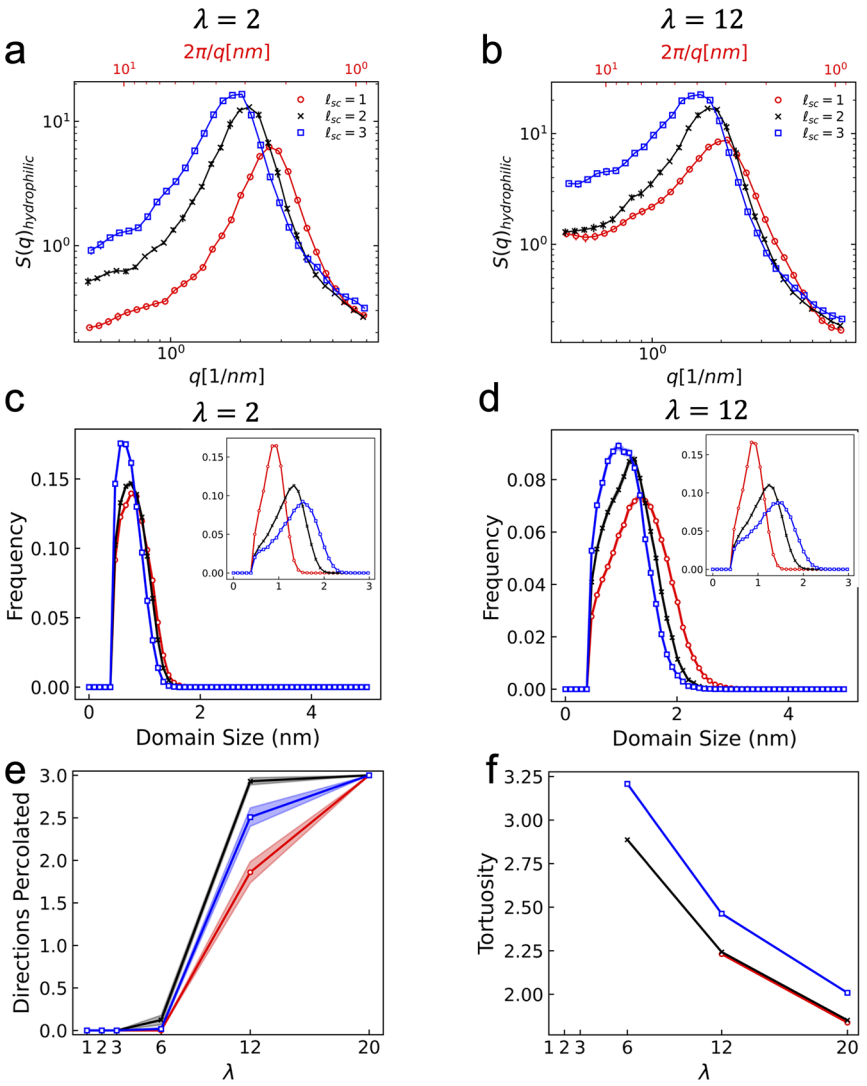

Figure 9. Results for ionomers with side chain spacing $\Gamma_{sc} = 4$ and varying side chain length. Partial structure factor of the hydrophilic components (water, sulfonate, and counterion beads) at $\lambda = 2$ (a) and $\lambda = 12$ (b). Hydrophilic domain size distributions for $\lambda = 2$ (c) and $\lambda = 12$ (d). Insets in (c) and (d) show the hydrophobic domain size distributions. (e) Plot of the hydrophilic domain directions percolated vs λ. (f) Plot of tortuosity of percolated hydrophilic vs λ.

increase in the low-q scattering intensity as compared to $\Gamma_{sc} = 2$ and 4; this increase in low-q scattering intensity for $\Gamma_{sc} = 8$ is the result of the formation of large (2−4 nm) hydrophilic domains that are not well-connected and isolated from each other (Figure S5 in Supporting Information). In the case of the binary blends with $\langle\Gamma_{sc}\rangle = 4$, the domains are similar in thickness to the monodisperse and polydisperse systems but have lower tortuosity and much higher propensity to percolate than the monodisperse and polydisperse systems. High percolation and low tortuosity are also seen in the monodisperse $\Gamma_{sc} = 2$ systems; however, they did not exhibit increased scattering intensity at low-q (Figure 7a,b) like the binary blends do. Additionally, the hydrophobic domain size distributions are similar between the binary blend systems (Figure 8c,d) and the monodisperse $\Gamma_{sc} = 2$ system (Figure 7c,d), with the binary blend systems being slightly larger. This leads us to the conclusion that there are fundamental differences in the hydrophilic domain structures between the monodisperse $\Gamma_{sc} = 2$ systems and the binary blends that are not seen in the hydrophilic domain size distribution, tortuosity, and onset of percolation but are present in the low-q scattering intensities.

From the above observations, we have learned two important lessons: (i) similar features in the scattering profile can arise from different features in the real-space domain structures, which means interpretation of scattering profiles has to take this "degeneracy" into consideration. (ii) Mixing ionomer designs within the same material either by blending of two populations of monodisperse chains or by introducing polydispersity in each chain can lead to fundamentally different domain structures whose features manifest differently in the scattering profiles. This underlies the limitations of interpreting scattering profiles using fits to traditional analytical models, and there is a need to develop more sophisticated real-space structural reconstructions that can quantify these subtle structural differences.

3.3. Effect of Varying Side Chain Length on Scattering Profiles and Real-Space Domain Structure. *3.3.1. Monodisperse Systems.* The length of the side chain determines the influence of the hydrophobic backbone on the local environment around the charged end groups, whereby increasing the side chain length allows the charge group to become more isolated from the hydrophobic backbone. By increasing or decreasing the distance between the charged end groups and

https://doi.org/10.1021/acs.macromol.4c00988
Macromolecules 2024, 57, 8223−8239

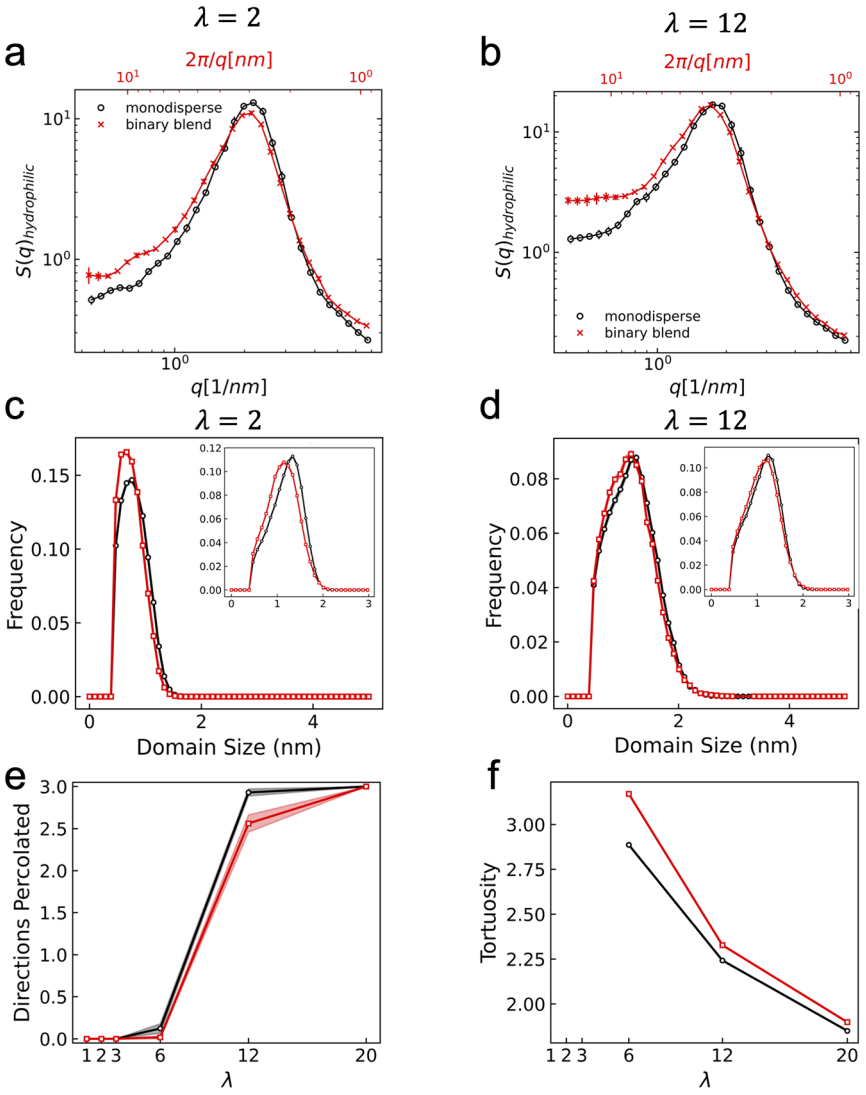

Figure 10. Results for ionomers with average side chain length $l_{sc} = 2$, including monomodal solution (black) and a binary mixture (red). The three binary mixtures are made up of chains with side chain lengths, $l_{sc}^{A} = 1$, and $l_{sc}^{B} = 3$, with fraction of chain A, $f_A = 0.5$. Partial structure factor of the hydrophilic components (water, sulfonate, and counterion beads) at $\lambda = 2$ (a) and $\lambda = 12$ (b). Hydrophilic domain size distributions for $\lambda = 2$ (c) and $\lambda = 12$ (d). Insets in (c) and (d) show the hydrophobic domain size distributions. (e) Plot of the hydrophilic domain directions percolated vs λ. (f) Plot of tortuosity of percolated hydrophilic vs λ.

backbone, the ability of water molecules to organize around the sulfonate end groups will change accordingly. As stated earlier, the variability in the side chain length inherently leads to differences in EW, and as shown in Section 2.4 of this paper as well as previously in other work,[45] changes in the EW can drastically affect the ionomer structure. Determining whether the changes observed upon varying the side chain length are due to the increase in distance between the sulfonate end group and the polymer backbone or simply due to changes in the mass ratio of dry polymer to sulfonate end groups (i.e., relative number of neutral beads to charged beads in CG ionomer) will require further study.

At low hydration (Figure 9a), the partial structure factor of the hydrophilic domains for varying side chain lengths of $l_{sc} = 1, 2, 3$ shows that increasing l_{sc} leads to an increase in the peak scattering intensity as well as a shift in the peak location toward smaller q-values. Increases in the scattering intensity in the low-q range are also observed with increasing l_{sc}. At low hydration, these changes in scattering intensities are most pronounced going from $l_{sc} = 1$ to $l_{sc} = 2$.

At high hydration (Figure 9b), $\lambda = 12$, the partial structure factor of the hydrophilic domains shows that increasing l_{sc} leads to an increase in the peak scattering intensity as well as a shift in the peak location toward smaller q-values. At low-q range, $l_{sc} = 3$ exhibits a higher scattering intensity than the lower two values of the side chain lengths.

With regard to the real-space hydrophilic domain size distribution, at low hydration (Figure 9c), the hydrophilic domain size distributions are similar between the three side chain lengths, with $l_{sc} = 1$ producing hydrophilic domains with the largest mean domain size, and $l_{sc} = 3$ producing hydrophilic domains with the smallest mean domain size. At high hydration (Figure 9d), the hydrophilic domain size distributions for $l_{sc} = 1$ shows hydrophilic domains that are substantially greater in size than the $l_{sc} = 2$ and $l_{sc} = 3$. In contrast, the spacing between the hydrophilic domains increases significantly with $l_{sc} = 1$ at both low and high hydration.

https://doi.org/10.1021/acs.macromol.4c00988
Macromolecules 2024, 57, 8223−8239

These results in Figure 9a−d show that as the hydration content is increased, the growth of the hydrophilic domains for ionomer chains with $l_{sc} = 1$ is more significant as compared to ionomer chains with $l_{sc} = 2$ and $l_{sc} = 3$. We observe that a large increase in the low-q scattering intensity can be a signature of significant growth of the domain sizes, although the results in the preceding section show that this correlation is not exclusive. We also observe that while the hydrophilic domain sizes show subtle variations that contrast the shift in ionomer peak q-value (shifts to higher q occur with increases in domain size), the more substantial difference in the spacing between the hydrophilic domains (i.e., hydrophobic domain sizes) better explains the ionomer peak shifts. Longer side chains lead to hydrophilic domains that are spaced further apart, explaining the shift of the ionomer peak to lower q.

Next, from the plot of the onset of percolation in each of the three dimensions (Figure 9e), we observe a similar onset of percolation for the three side chain lengths, but with $l_{sc} = 2$ having the most propensity for percolation and $l_{sc} = 1$ having the least propensity for percolation. While the mean domain size decreased with increasing l_{sc}, the onset of percolation is nonmonotonic with respect to l_{sc}. This is due to $l_{sc} = 1$ having the lowest propensity for percolation despite having the largest hydrophilic domain sizes and smallest hydrophilic domain spacing.

The tortuosity of the percolated hydrophilic domains (Figure 9f) shows a monotonic relationship between tortuosity and side chain length, with $l_{sc} = 3$ having the highest tortuosity. If we compared the tortuosity metrics generated upon changing side chain spacing (Figure 7) and changing side chain length (Figure 9), we find some interesting results. Increasing side chain spacing of the polymer led to drastic changes in tortuosity values from 1.7 to 5.0 at $\lambda = 12$ (Figure 7f). In contrast, increasing side chain length led to minimal changes in tortuosity from 2.2 to 3.5 at $\lambda = 12$ (Figure 9f). Further, as shown in Table 1 where we connect the EW values to the values of side chain spacing and length that we consider, the increase in EW values is more drastic with increasing side chain spacing than it is with increasing side chain length. Comparing the tortuosity values of increasing EW values, we can conclude that increasing EW leads to an increasing tortuosity.

3.3.2. Mixing Side Chain Lengths in the 50:50 Binary Blend. To determine if mixing ionomers with different side chain lengths can alter the hydrophilic domain structures as compared to the analogous monodisperse system, we modeled one binary blend with an average side chain length of $\langle l_{sc} \rangle = 2$, composed of a 50:50 blend of ionomers with $l_{sc}{}^{A} = 1$ and $l_{sc}{}^{B} = 3$.

Figure 10a,b shows that at both low and high hydration, the monodisperse systems $l_{sc} = 2$ show a narrower peak with the peak location at a higher q-value and slightly higher peak intensity as compared to the binary blend with $\langle l_{sc} \rangle = 2$. The low q-range scattering intensity is substantially higher for the blend as compared to that for the monodisperse system; this is similar to our observations when comparing the blends of ionomers with different side chain spacing to their monodisperse counterpart. The cause for this increase in the low-q scattering intensity is not clear as the hydrophilic domain size distribution measurements show similar size distributions between the monodisperse and binary blend, with the former having a slightly higher mean domain size at low hydration (Figure 10c) and at high hydration (Figure 10d). The hydrophobic domain size distributions (Figure 10c,d, insets) also show only a small shift to smaller sizes for the binary blends when compared to that for the monodisperse system. The tortuosity and onset of percolation between the two systems are similar, with the monodisperse system having a slightly higher propensity for percolation and slightly lower tortuosity (Figure 10e,f). In the previous section, we observed that the ionomers with $l_{sc} = 1$ had substantially larger structures at high hydration though the changes to the onset of percolation and tortuosity of the hydrophilic domains were similar to the other two side chain lengths. In the blend, we do not observe the emergence of the large hydrophilic domain structures observed in the monomodal solution with $l_{sc} = 1$ at high hydration, yet the low q-range scattering intensity is high for the blend as is the case for monodispersed $l_{sc} = 1$. The decrease in percolation propensity and increase in tortuosity seen in the blended systems as compared to that in the monodispersed system coincide with a decrease in the spacing between the hydrophilic domains (i.e., decreasing hydrophobic domain sizes), suggesting the decrease in connectivity is not due to the hydrophilic domains becoming more isolated from one another.

4. CONCLUSIONS

Understanding design rules for ionomers and having the ability to interpret the significance of features in the measured scattering profiles are both crucial steps needed for developing new and improved ionomer materials. In this study, we investigated the effects of varying the design of ionomer chains on the hydrophilic domain's morphology at various hydration contents with emphasis toward relating hydrophilic components' scattering profiles to the real-space structural features of the hydrophilic domains. Here are key conclusions from our study:

(i) Changing the ionomer designs and hydration content leads to observable changes in the scattering profile of the hydrophilic components, but how these changes are linked to the real-space hydrophilic domain properties is nontrivial. The trends observed in the real-space structural analysis with changing design does not necessarily match the trends observed in the scattering profiles; for instance, the scattering profile for $l_{sc} = 3$ shows a substantial increase in low-q scattering intensity when the hydration content is increased from $\lambda = 2$ to $\lambda = 12$ despite the hydrophobic domain size distribution shifting toward smaller sizes for both side chain lengths and the hydrophilic domain size distribution showing modest growth toward moderate domain size (∼2 nm) with the increase in hydration. This motivates the need to perform real-space analysis on the structures that are more sensitive to subtle variations at the intradomain and interdomain levels. In addition to employing alternate real-space structural analysis from simulations to interpret scattering profiles, we believe data-driven computational methods are needed to deconvolute the variations observed in the scattering profiles to real-space changes in hydrophilic domain structures.

(ii) Our study shows that blending ionomers with a side chain spacing $\Gamma_{sc} = 2$ with ionomers with $\Gamma_{sc} > 4$ to achieve an average spacing of $\langle \Gamma_{sc} \rangle = 4$ leads to hydrophilic domains with variable structures as compared to monodisperse ionomers with $\Gamma_{sc} = 4$. This suggests that blending ionomers could be a viable approach for altering the morphologies of the hydrophilic domains of hydrated

https://doi.org/10.1021/acs.macromol.4c00988
Macromolecules 2024, 57, 8223−8239

ionomers. In contrast, polydispersity in side chain spacing within the ionomer chains did not alter the structure from that seen in analogous monodisperse system with same average side chain spacing.

(iii) Studies of ionomer side chain length show some microstructural differences; these include variable tortuosity as well as variable hydration states required for percolation. Ionomers with short side chain length of $l_{sc} = 1$ seemed to demonstrate larger ionic domains; however, they had the least propensity for percolation. When comparing 50:50 blends of ionomers with two side chain lengths, with a mean side chain length of $\langle l_{sc} \rangle = 2$ to the monodisperse $l_{sc} = 2$ system, we find similar domain size distributions, onset of percolation, and tortuosity of the hydrophilic domains. Yet, there are significant variations in the binary blend and monodisperse systems' scattering profiles, particularly in the low q-range scattering intensities. The explanation for why there is a difference in the low-q intensities without any obvious differences in our real-space structure analyses is elusive at this time.

■ ASSOCIATED CONTENT

Supporting Information

The Supporting Information is available free of charge at https://pubs.acs.org/doi/10.1021/acs.macromol.4c00988.

Simulation parameters and additional simulation analysis, effect of the scattering length density values used in the calculation of structure factors, and comparison of results obtained from simulations using polarizable water beads vs. nonpolarizable water beads (PDF)

■ AUTHOR INFORMATION

Corresponding Author

Arthi Jayaraman − *Department of Chemical and Biomolecular Engineering, University of Delaware, Newark, Delaware 19716, United States; Department of Materials Science and Engineering, University of Delaware, Newark, Delaware 19716, United States;* orcid.org/0000-0002-5295-4581; Email: arthij@udel.edu

Authors

Jason J. Madinya − *Department of Chemical and Biomolecular Engineering, University of Delaware, Newark, Delaware 19716, United States;* orcid.org/0000-0002-1401-8098

Stephen Kronenberger − *Department of Chemical and Biomolecular Engineering, University of Delaware, Newark, Delaware 19716, United States;* orcid.org/0000-0002-7084-4060

Benjamin Gould − *The Chemours Company, Newark, Delaware 19713, United States*

Colin Peterson − *The Chemours Company, Newark, Delaware 19713, United States*

Complete contact information is available at: https://pubs.acs.org/10.1021/acs.macromol.4c00988

Author Contributions

A.J. secured the funding to support this work. J.M. conducted the coarse-grained simulations. S.K. developed analysis algorithms for both S.K. and J.M. to quantify the structural analyses on the simulated configurations. J.M., S.K., and A.J. wrote and edited the manuscript.

Notes

The authors declare no competing financial interest.

■ ACKNOWLEDGMENTS

JM acknowledges funding from NSF MPS-Ascend Postdoctoral Research Fellowship under grant no. 2316666. S.K. and A.J. acknowledge support from NSF-NRT Computing and Data Science Training for Materials Innovation, Discovery, Analytics program under grant DGE 2125703 for fellowship that supported S.K. A.J. is grateful for financial support from Chemours Company that partially supported this project. This research was supported in part through the use of Information Technologies (IT) resources at the University of Delaware, including the high-performance computing resources of the DARWIN supercomputing cluster. Additionally, this work used the BRIDGES 2 supercomputer at Pittsburgh Supercomputing Center through allocation MCB100140. All authors thank Nitant Gupta for his insightful input and contributions.

■ REFERENCES

(1) Zhang, L.; Brostowitz, N. R.; Cavicchi, K. A.; Weiss, R. A. Perspective: Ionomer Research and Applications. *Macromol. React. Eng.* **2014**, *8* (2), 81−99.

(2) Zhang, Z.; Liu, C.; Cao, X.; Wang, J.-H. H.; Chen, Q.; Colby, R. H. Morphological Evolution of Ionomer/Plasticizer Mixtures during a Transition from Ionomer to Polyelectrolyte. *Macromolecules* **2017**, *50* (3), 963−971.

(3) Bollinger, J. A.; Stevens, M. J.; Frischknecht, A. L. Quantifying Single-Ion Transport in Percolated Ionic Aggregates of Polymer Melts. *ACS Macro Lett.* **2020**, *9* (4), 583−587.

(4) Ling, G. H.; Wang, Y.; Weiss, R. A. Linear Viscoelastic and Uniaxial Extensional Rheology of Alkali Metal Neutralized Sulfonated Oligostyrene Ionomer Melts. *Macromolecules* **2012**, *45* (1), 481−490.

(5) Weiss, R. A.; Zhao, H. Rheological behavior of oligomeric ionomers. *J. Rheol.* **2009**, *53* (1), 191−213.

(6) Wu, D.; Paddison, S. J.; Elliott, J. A. A comparative study of the hydrated morphologies of perfluorosulfonic acid fuel cell membranes with mesoscopic simulations. *Energy Environ. Sci.* **2008**, *1* (2), 284−293.

(7) Freger, V. Hydration of Ionomers and Schroeder's Paradox in Nafion. *J. Phys. Chem. B* **2009**, *113* (1), 24−36.

(8) Hristov, I. H.; Paddison, S. J.; Paul, R. Molecular Modeling of Proton Transport in the Short-Side-Chain Perfluorosulfonic Acid Ionomer. *J. Phys. Chem. B* **2008**, *112* (10), 2937−2949.

(9) Chang, Y.; Brunello, G. F.; Fuller, J.; Hawley, M.; Kim, Y. S.; Disabb-Miller, M.; Hickner, M. A.; Jang, S. S.; Bae, C. Aromatic Ionomers with Highly Acidic Sulfonate Groups: Acidity, Hydration, and Proton Conductivity. *Macromolecules* **2011**, *44* (21), 8458−8469.

(10) Wang, C.; Paddison, S. J. Mesoscale modeling of hydrated morphologies of sulfonated polysulfone ionomers. *Soft Matter* **2014**, *10* (6), 819−830.

(11) Wang, C.; Krishnan, V.; Wu, D.; Bledsoe, R.; Paddison, S. J.; Duscher, G. Evaluation of the microstructure of dry and hydrated perfluorosulfonic acid ionomers: microscopy and simulations. *J. Mater. Chem. A* **2013**, *1* (3), 938−944.

(12) Esmaeilirad, M.; Jiang, Z.; Harzandi, A. M.; Kondori, A.; Tamadoni Saray, M.; Segre, C. U.; Shahbazian-Yassar, R.; Rappe, A. M.; Asadi, M. Imidazolium-functionalized Mo3P nanoparticles with an ionomer coating for electrocatalytic reduction of CO2 to propane. *Nat. Energy* **2023**, *8* (8), 891−900.

(13) Kim, C.; Bui, J. C.; Luo, X.; Cooper, J. K.; Kusoglu, A.; Weber, A. Z.; Bell, A. T. Tailored catalyst microenvironments for CO2 electroreduction to multicarbon products on copper using bilayer ionomer coatings. *Nat. Energy* **2021**, *6* (11), 1026−1034.

(14) Morselli, D.; Cataldi, P.; Paul, U. C.; Ceseracciu, L.; Benitez, J. J.; Scarpellini, A.; Guzman-Puyol, S.; Heredia, A.; Valentini, P.; Pompa, P. P.; et al. Zinc Polyaleuritate Ionomer Coatings as a Sustainable,

Alternative Technology for Bisphenol A-Free Metal Packaging. *ACS Sustainable Chem. Eng.* **2021**, *9* (46), 15484−15495.
(15) Dolog, R.; Weiss, R. A. Shape Memory Behavior of a Polyethylene-Based Carboxylate Ionomer. *Macromolecules* **2013**, *46* (19), 7845−7852.
(16) Lu, L.; Li, G. One-Way Multishape-Memory Effect and Tunable Two-Way Shape Memory Effect of Ionomer Poly(ethylene-co-methacrylic acid). *ACS Appl. Mater. Interfaces* **2016**, *8* (23), 14812−14823.
(17) Bronich, T. K.; Nehls, A.; Eisenberg, A.; Kabanov, V. A.; Kabanov, A. V. Novel drug delivery systems based on the complexes of block ionomers and surfactants of opposite charge. *Colloids Surf., B* **1999**, *16* (1−4), 243−251.
(18) Kabanov, A. V.; Kabanov, V. A. Interpolyelectrolyte and block ionomer complexes for gene delivery: physico-chemical aspects. *Adv. Drug Delivery Rev.* **1998**, *30* (1−3), 49−60.
(19) Oh, K. T.; Bronich, T. K.; Bromberg, L.; Hatton, T. A.; Kabanov, A. V. Block ionomer complexes as prospective nanocontainers for drug delivery. *J. Controlled Release* **2006**, *115* (1), 9−17.
(20) Kerres, J. A. Development of ionomer membranes for fuel cells. *J. Membr. Sci.* **2001**, *185* (1), 3−27.
(21) Morawietz, T.; Handl, M.; Oldani, C.; Friedrich, K. A.; Hiesgen, R. Quantitative in Situ Analysis of Ionomer Structure in Fuel Cell Catalytic Layers. *ACS Appl. Mater. Interfaces* **2016**, *8* (40), 27044−27054.
(22) Asano, N.; Miyatake, K.; Watanabe, M. Hydrolytically Stable Polyimide Ionomer for Fuel Cell Applications. *Chem. Mater.* **2004**, *16* (15), 2841−2843.
(23) Gu, S.; Cai, R.; Luo, T.; Chen, Z.; Sun, M.; Liu, Y.; He, G.; Yan, Y. A Soluble and Highly Conductive Ionomer for High-Performance Hydroxide Exchange Membrane Fuel Cells. *Angew. Chem., Int. Ed.* **2009**, *48* (35), 6499−6502.
(24) Asano, N.; Aoki, M.; Suzuki, S.; Miyatake, K.; Uchida, H.; Watanabe, M. Aliphatic/Aromatic Polyimide Ionomers as a Proton Conductive Membrane for Fuel Cell Applications. *J. Am. Chem. Soc.* **2006**, *128* (5), 1762−1769.
(25) Faid, A. Y.; Xie, L.; Barnett, A. O.; Seland, F.; Kirk, D.; Sunde, S. Effect of anion exchange ionomer content on electrode performance in AEM water electrolysis. *Int. J. Hydrogen Energy* **2020**, *45* (53), 28272−28284.
(26) Krivina, R. A.; Lindquist, G. A.; Beaudoin, S. R.; Stovall, T. N.; Thompson, W. L.; Twight, L. P.; Marsh, D.; Grzyb, J.; Fabrizio, K.; Hutchison, J. E.; Boettcher, S. W. Anode Catalysts in Anion-Exchange-Membrane Electrolysis without Supporting Electrolyte: Conductivity, Dynamics, and Ionomer Degradation. *Adv. Mater.* **2022**, *34* (35), 2203033.
(27) Smith, D. W.; Oladoyinbo, F. O.; Mortimore, W. A.; Colquhoun, H. M.; Thomassen, M. S.; Ødegård, A.; Guillet, N.; Mayousse, E.; Klicpera, T.; Hayes, W. A Microblock Ionomer in Proton Exchange Membrane Electrolysis for the Production of High Purity Hydrogen. *Macromolecules* **2013**, *46* (4), 1504−1511.
(28) Kim, J. Q.; So, S.; Kim, H.-T.; Choi, S. Q. Highly Ordered Ultrathin Perfluorinated Sulfonic Acid Ionomer Membranes for Vanadium Redox Flow Battery. *ACS Energy Lett.* **2021**, *6* (1), 184−192.
(29) Chen, D.; Wang, S.; Xiao, M.; Meng, Y. Synthesis and characterization of novel sulfonated poly(arylene thioether) ionomers for vanadium redox flow battery applications. *Energy Environ. Sci.* **2010**, *3* (5), 622−628.
(30) Palanisamy, G.; Sadhasivam, T.; Park, W.-S.; Bae, S. T.; Roh, S.-H.; Jung, H.-Y. Tuning the Ion Selectivity and Chemical Stability of a Biocellulose Membrane by PFSA Ionomer Reinforcement for Vanadium Redox Flow Battery Applications. *ACS Sustainable Chem. Eng.* **2020**, *8* (4), 2040−2051.
(31) Matsuyama, H.; Matsui, K.; Kitamura, Y.; Maki, T.; Teramoto, M. Effects of membrane thickness and membrane preparation condition on facilitated transport of CO2 through ionomer membrane. *Sep. Purif. Technol.* **1999**, *17* (3), 235−241.
(32) Koval, C. A.; Spontarelli, T.; Noble, R. D. Styrene/ethylbenzene separation using facilitated transport through perfluorosulfonate ionomer membranes. *Ind. Eng. Chem. Res.* **1989**, *28* (7), 1020−1024.
(33) Kusoglu, A.; Weber, A. Z. New Insights into Perfluorinated Sulfonic-Acid Ionomers. *Chem. Rev.* **2017**, *117* (3), 987−1104.
(34) Rollet, A.-L.; Diat, O.; Gebel, G. A New Insight into Nafion Structure. *J. Phys. Chem. B* **2002**, *106* (12), 3033−3036.
(35) Xue, T.; Trent, J. S.; Osseo-Asare, K. Characterization of nafion® membranes by transmission electron microscopy. *J. Membr. Sci.* **1989**, *45* (3), 261−271.
(36) Porat, Z. e.; Fryer, J. R.; Huxham, M.; Rubinstein, I. Electron Microscopy Investigation of the Microstructure of Nafion Films. *J. Phys. Chem.* **1995**, *99* (13), 4667−4671.
(37) Rieberer, S.; Norian, K. H. Analytical electron microscopy of Nafion ion exchange membranes. *Ultramicroscopy* **1992**, *41* (1−3), 225−233.
(38) McLean, R. S.; Doyle, M.; Sauer, B. B. High-Resolution Imaging of Ionic Domains and Crystal Morphology in Ionomers Using AFM Techniques. *Macromolecules* **2000**, *33* (17), 6541−6550.
(39) Mauritz, K. A.; Moore, R. B. State of Understanding of Nafion. *Chem. Rev.* **2004**, *104* (10), 4535−4586.
(40) Fujimura, M.; Hashimoto, T.; Kawai, H. Small-angle x-ray scattering study of perfluorinated ionomer membranes. 1. Origin of two scattering maxima. *Macromolecules* **1981**, *14* (5), 1309−1315.
(41) Gebel, G.; Moore, R. B. Small-Angle Scattering Study of Short Pendant Chain Perfluorosulfonated Ionomer Membranes. *Macromolecules* **2000**, *33* (13), 4850−4855.
(42) Moore, R. B.; Martin, C. R., III Morphology and chemical properties of the Dow perfluorosulfonate ionomers. *Macromolecules* **1989**, *22* (9), 3594−3599.
(43) Kusoglu, A.; Dursch, T. J.; Weber, A. Z. Nanostructure/Swelling Relationships of Bulk and Thin-Film PFSA Ionomers. *Adv. Funct. Mater.* **2016**, *26* (27), 4961−4975.
(44) Kuo, A.-T.; Shinoda, W.; Okazaki, S. Molecular Dynamics Study of the Morphology of Hydrated Perfluorosulfonic Acid Polymer Membranes. *J. Phys. Chem. C* **2016**, *120* (45), 25832−25842.
(45) Kuo, A.-T.; Takeuchi, K.; Tanaka, A.; Urata, S.; Okazaki, S.; Shinoda, W. Exploring the effect of pendent side chain length on the structural and mechanical properties of hydrated perfluorosulfonic acid polymer membranes by molecular dynamics simulation. *Polymer* **2018**, *146*, 53−62.
(46) Liu, H.; Cavaliere, S.; Jones, D. J.; Rozière, J.; Paddison, S. J. Morphology of Hydrated Nafion through a Quantitative Cluster Analysis: A Case Study Based on Dissipative Particle Dynamics Simulations. *J. Phys. Chem. C* **2018**, *122* (24), 13130−13139.
(47) Marrink, S. J.; Risselada, H. J.; Yefimov, S.; Tieleman, D. P.; de Vries, A. H. The MARTINI Force Field: Coarse Grained Model for Biomolecular Simulations. *J. Phys. Chem. B* **2007**, *111* (27), 7812−7824.
(48) Monticelli, L.; Kandasamy, S. K.; Periole, X.; Larson, R. G.; Tieleman, D. P.; Marrink, S.-J. The MARTINI Coarse-Grained Force Field: Extension to Proteins. *J. Chem. Theory Comput.* **2008**, *4* (5), 819−834.
(49) de Jong, D. H.; Singh, G.; Bennett, W. F. D.; Arnarez, C.; Wassenaar, T. A.; Schäfer, L. V.; Periole, X.; Tieleman, D. P.; Marrink, S. J. Improved Parameters for the Martini Coarse-Grained Protein Force Field. *J. Chem. Theory Comput.* **2013**, *9* (1), 687−697.
(50) Mabuchi, T.; Tokumasu, T. Ionomer Dispersions in Water/Alcohol Solutions by Coarse-Grained Molecular Dynamics. *ECS Trans.* **2017**, *80* (8), 577−581.
(51) Michalowsky, J.; Schäfer, L. V.; Holm, C.; Smiatek, J. A refined polarizable water model for the coarse-grained MARTINI force field with long-range electrostatic interactions. *J. Chem. Phys.* **2017**, *146* (5), 054501.
(52) Mabuchi, T.; Huang, S.-F.; Tokumasu, T. Nafion Ionomer Dispersion in Mixtures of 1-Propanol and Water Based on the Martini Coarse-Grained Model. *J. Polym. Sci.* **2020**, *58* (3), 487−499.
(53) Mabuchi, T.; Huang, S.-F.; Tokumasu, T. Dispersion of Nafion Ionomer Aggregates in 1-Propanol/Water Solutions: Effects of

https://doi.org/10.1021/acs.macromol.4c00988
Macromolecules 2024, 57, 8223−8239

Ionomer Concentration, Alcohol Content, and Salt Addition. *Macromolecules* **2020**, *53* (9), 3273−3283.
(54) Mabuchi, T.; Huang, S.-F.; Tokumasu, T. Influence of Ionomer Loading and Substrate Wettability on the Morphology of Ionomer Thin Films Using Coarse-Grained Solvent Evaporation Simulations. *Macromolecules* **2021**, *54* (1), 115−125.
(55) Abraham, M.; Alekseenko, A.; Bergh, C.; Blau, C.; Briand, E.; Doijade, M.; Fleischmann, S.; Gapsys, V.; Garg, G.; Gorelov, S.; et al. *GROMACS 2023.3 Manual*, 2023..
(56) Brisard, S.; Levitz, P. Small-angle scattering of dense, polydisperse granular porous media: Computation free of size effects. *Phys. Rev. E: Stat., Nonlinear, Soft Matter Phys.* **2013**, *87* (1), 013305.
(57) Hagberg, A. A.; Schult, D. A.; Swart, P. J.. In *Exploring Network Structure, Dynamics, and Function using NetworkX*, 2008.
(58) Gostick, J. T.; Khan, Z. A.; Tranter, T. G.; Kok, M. D. r.; Agnaou, M.; Sadeghi, M.; Jervis, R. PoreSpy: A Python Toolkit for Quantitative Analysis of Porous Media Images. *J. Open Source Softw.* **2019**, *4* (37), 1296.
(59) Wang, K. W.; Betancourt, T.; Hall, C. K. Computational study of DNA-cross-linked hydrogel formation for drug delivery applications. *Macromolecules* **2018**, *51* (23), 9758−9768.
(60) Bhattacharya, S.; Gubbins, K. E. Fast Method for Computing Pore Size Distributions of Model Materials. *Langmuir* **2006**, *22* (18), 7726−7731.
(61) Ramaswamy, N.; Kumaraguru, S.; Koestner, R.; Fuller, T.; Gu, W.; Kariuki, N.; Myers, D.; Dudenas, P. J.; Kusoglu, A. Editors' Choice—Ionomer Side Chain Length and Equivalent Weight Impact on High Current Density Transport Resistances in PEMFC Cathodes. *J. Electrochem. Soc.* **2021**, *168* (2), 024518.
(62) Sorte, E. G.; Paren, B. A.; Rodriguez, C. G.; Fujimoto, C.; Poirier, C.; Abbott, L. J.; Lynd, N. A.; Winey, K. I.; Frischknecht, A. L.; Alam, T. M. Impact of Hydration and Sulfonation on the Morphology and Ionic Conductivity of Sulfonated Poly(phenylene) Proton Exchange Membranes. *Macromolecules* **2019**, *52* (3), 857−876.
(63) Knauth, P.; Pasquini, L.; Narducci, R.; Sgreccia, E.; Becerra-Arciniegas, R. A.; Di Vona, M. L. Effective ion mobility in anion exchange ionomers: Relations with hydration, porosity, tortuosity, and percolation. *J. Membr. Sci.* **2021**, *617*, 118622.
(64) Epstein, N. On tortuosity and the tortuosity factor in flow and diffusion through porous media. *Chem. Eng. Sci.* **1989**, *44* (3), 777−779.
(65) Wernert, V.; Bouchet, R.; Denoyel, R. Influence of Molecule Size on Its Transport Properties through a Porous Medium. *Anal. Chem.* **2010**, *82* (7), 2668−2679.
(66) Win, M. S.; Winey, K. I.; Frischknecht, A. L. Morphology-Diffusivity Relationships in Fluorine-Free Random Terpolymers for Proton-Exchange Membranes. *Macromolecules* **2023**, *56* (23), 9905−9913.

https://doi.org/10.1021/acs.macromol.4c00988
Macromolecules 2024, 57, 8223−8239